The Astrophysical Journal, 932:40 (19pp), 2022 June 10 https://doi.org/10.3847/1538-4357/ac6c29

In Search of Short Gamma-Ray Burst Optical Counterparts with the Zwicky Transient Facility

Tomás Ahumada[1,2,3,41], Shreya Anand[4], Michael W. Coughlin[5], Igor Andreoni[1,2,6], Erik C. Kool[7], Harsh Kumar[8,9], Simeon Reusch[10,11], Ana Sagués-Carracedo[12], Robert Stein[4,10,11], S. Bradley Cenko[2,6], Mansi M. Kasliwal[4], Leo P. Singer[2,6], Rachel Dunwoody[13], Joseph Mangan[13], Varun Bhalerao[8], Mattia Bulla[7], Eric Burns[14], Matthew J. Graham[4], David L. Kaplan[15], Daniel Perley[16], Mouza Almualla[17], Joshua S. Bloom[18,19], Virginia Cunningham[20], Kishalay De[21], Pradip Gatkine[4], Anna Y. Q. Ho[22,23,24], Viraj Karambelkar[4], Albert K. H. Kong[25], Yuhan Yao[4], G. C. Anupama[26], Sudhanshu Barway[26], Shaon Ghosh[27,28], Ryosuke Itoh[29], Sheila McBreen[13], Eric C. Bellm[30], Christoffer Fremling[4], Russ R. Laher[31], Ashish A. Mahabal[4,32], Reed L. Riddle[33], Philippe Rosnet[34], Ben Rusholme[31], Roger Smith[33], Jesper Sollerman[7], Elisabetta Bissaldi[35,36], Corinne Fletcher[37], Rachel Hamburg[38], Bagrat Mailyan[39], Christian Malacaria[40], and Oliver Roberts[37]

[1] Department of Astronomy, University of Maryland, College Park, MD 20742, USA; tahumada@astro.umd.edu
[2] Astrophysics Science Division, NASA Goddard Space Flight Center, MC 661, Greenbelt, MD 20771, USA
[3] Center for Research and Exploration in Space Science and Technology, NASA Goddard Space Flight Center, Greenbelt, MD 20771, USA
[4] Division of Physics, Mathematics and Astronomy, California Institute of Technology, Pasadena, CA 91125, USA
[5] School of Physics and Astronomy, University of Minnesota, Minneapolis, MN 55455, USA
[6] Joint Space-Science Institute, University of Maryland, College Park, MD 20742, USA
[7] The Oskar Klein Centre, Department of Astronomy, Stockholm University, AlbaNova, SE-10691, Stockholm, Sweden
[8] Department of Physics, Indian Institute of Technology Bombay, Powai, Mumbai 400076, India
[9] LSSTC Data Science Fellow 2018
[10] Deutsches Elektronen Synchrotron DESY, Platanenallee 6, D-15738 Zeuthen, Germany
[11] Institut für Physik, Humboldt-Universität zu Berlin, D-12489 Berlin, Germany
[12] The Oskar Klein Centre, Department of Physics, Stockholm University, AlbaNova, SE-106 91 Stockholm, Sweden
[13] School of Physics, University College Dublin, Dublin 4, Ireland
[14] Department of Physics and Astronomy, Louisiana State University, Baton Rouge, LA 70803, USA
[15] Center for Gravitation, Cosmology and Astrophysics, Department of Physics, University of Wisconsin–Milwaukee, P.O. Box 413, Milwaukee, WI 53201, USA
[16] Astrophysics Research Institute, Liverpool John Moores University, IC2, Liverpool Science Park, 146 Brownlow Hill, Liverpool L3 5RF, UK
[17] American University of Sharjah, Physics Department, PO Box 26666, Sharjah, UAE
[18] Department of Astronomy, University of California, Berkeley, CA 94720-3411, USA
[19] Lawrence Berkeley National Laboratory, 1 Cyclotron Road, MS 50B-4206, Berkeley, CA 94720-3411, USA
[20] Space Telescope Science Institute, 3700 San Martin Dr., Baltimore, MD 21218, USA
[21] MIT-Kavli Institute for Astrophysics and Space Research, 77 Massachusetts Ave., Cambridge, MA 02139, USA
[22] Miller Institute for Basic Research in Science, 468 Donner Lab, Berkeley, CA 94720, USA
[23] Department of Astronomy, University of California, Berkeley, Berkeley, CA 94720, USA
[24] Lawrence Berkeley National Laboratory, 1 Cyclotron Road, MS 50B-4206, Berkeley, CA 94720, USA
[25] Institute of Astronomy, National Tsing Hua University, Hsinchu 300044, Taiwan
[26] Indian Institute of Astrophysics, II Block Koramangala, Bengaluru 560034, India
[27] Montclair State University, 1 Normal Ave., Montclair, NJ 07043, USA
[28] University of Wisconsin-Milwaukee, Milwaukee, WI 53201, USA
[29] Bisei Astronomical Observatory, 1723-70 Ookura, Bisei-cho, Ibara, Okayama 714-1411, Japan
[30] DIRAC Institute, Department of Astronomy, University of Washington, 3910 15th Avenue NE, Seattle, WA 98195, USA
[31] IPAC, California Institute of Technology, 1200 E. California Blvd, Pasadena, CA 91125, USA
[32] Center for Data Driven Discovery, California Institute of Technology, Pasadena, CA 91125, USA
[33] Caltech Optical Observatories, California Institute of Technology, Pasadena, CA 91125, USA
[34] Université Clermont Auvergne, CNRS/IN2P3, LPC, F-63000 Clermont-Ferrand, France
[35] Dipartimento di Fisica "M. Merlin" dell'Universit`a e del Politecnico di Bari, I-70126 Bari, Italy
[36] Istituto Nazionale di Fisica Nucleare, Sezione di Bari, I-70126 Bari, Italy
[37] Science and Technology Institute, Universities Space Research Association, Huntsville, AL 35805, USA
[38] Space Science Department, University of Alabama in Huntsville, 320 Sparkman Drive, Huntsville, AL 35899, USA
[39] Center for Space Plasma and Aeronomic Research, University of Alabama in Huntsville, 320 Sparkman Drive, Huntsville, AL 35899, USA
[40] Astrophysics Office, ST12, NASA/Marshall Space Flight Center, Huntsville, AL 35812, USA
Received 2022 March 21; revised 2022 April 21; accepted 2022 May 1; published 2022 June 14

Abstract

The Fermi Gamma-ray Burst Monitor (GBM) triggers on-board in response to ∼40 short gamma-ray bursts (SGRBs) per year; however, their large localization regions have made the search for optical counterparts a challenging endeavour. We have developed and executed an extensive program with the wide field of view of the Zwicky Transient Facility (ZTF) camera, mounted on the Palomar 48 inch Oschin telescope (P48), to perform

[41] LSSTC Data Science Fellow.

target-of-opportunity (ToO) observations on 10 Fermi-GBM SGRBs during 2018 and 2020–2021. Bridging the large sky areas with small field-of-view optical telescopes in order to track the evolution of potential candidates, we look for the elusive SGRB afterglows and kilonovae (KNe) associated with these high-energy events. No counterpart has yet been found, even though more than 10 ground-based telescopes, part of the Global Relay of Observatories Watching Transients Happen (GROWTH) network, have taken part in these efforts. The candidate selection procedure and the follow-up strategy have shown that ZTF is an efficient instrument for searching for poorly localized SGRBs, retrieving a reasonable number of candidates to follow up and showing promising capabilities as the community approaches the multi-messenger era. Based on the median limiting magnitude of ZTF, our searches would have been able to retrieve a GW170817-like event up to ∼200 Mpc and SGRB afterglows to $z = 0.16$ or 0.4, depending on the assumed underlying energy model. Future ToOs will expand the horizon to $z = 0.2$ and 0.7, respectively.

Unified Astronomy Thesaurus concepts: Gamma-ray bursts (629); Wide-field telescopes (1800)

1. Introduction

Between the years 1969–1972, the Vela Satellites discovered (GRBs) and further analysis confirmed their cosmic origin (Klebesadel et al. 1973). These GRBs are among the brightest events in the universe, and have been observed both in nearby galaxies as well as at cosmological distances (Metzger et al. 1997). The data collected over the years suggest a bimodal distribution in the time duration of the GRB that distinguishes two groups: long GRBs (LGRB; $T_{90} > 2s$) and short GRBs (SGRB; $T_{90} < 2s$) (Kouveliotou et al. 1993), where T_{90} is defined as the duration that encloses the 5th to the 95th percentiles of fluence or counts, depending on the instrument.

LGRBs have been associated with supernova (SN) explosions (Bloom et al. 1999; Woosley & Bloom 2006) and a large number of them have counterparts at longer wavelengths (Cano et al. 2017). On the other hand, only ∼35 SGRBs have optical/NIR detections (Fong et al. 2015; Rastinejad et al. 2021), thus their progenitors are still an active area of research. SGRBs have been shown to occur in environments with old populations of stars (Berger et al. 2005; D'Avanzo 2015) and have long been linked with mergers of compact binaries, such as binary neutron star (BNS) and neutron star-black hole (NSBH) (Narayan et al. 1992). The discovery of the gravitational-wave event GW170817 coincident with the short gamma-ray burst, GRB 170817A, unambiguously confirmed BNS mergers as at least one of the mechanisms that can produce a SGRB (Abbott et al. 2017a). However, compact binary mergers might not be the only source of SGRBs, as collapsars (Ahumada et al. 2021; Zhang et al. 2021) and giant flares from magnetars (Burns et al. 2021) can masquerade as short-duration GRBs. Hence, the traditional classification of a burst based solely on the time duration is subject to debate (Zhang 2008; Bromberg et al. 2013; Amati 2021). For example, other gamma-ray properties (i.e., the hardness ratio) can cluster the bursts in different populations (Nakar 2007), and there are a couple of examples for which the time classification of the burst has been questioned due to the presence or lack of SN emissions (Gal-Yam et al. 2006; Ahumada et al. 2021; Rossi et al. 2021; Zhang et al. 2021). In this context, the search for the optical counterparts of SGRBs is essential to unveil the nature of their progenitors and the underlying physics.

Not all SGRBs show similar gamma-ray features and different models have tried to explain the observations. For example, the "fireball" model (Wijers et al. 1997; Mészáros and Rees 1998; Piran 1999; Zhang 2013) describes a highly relativistic jet of charged particle plasma emitted by a compact central engine as a result of a BNS or NSBH merger. The model predicts the production of gamma-rays and hard X-rays within the jet. The interaction of the jet and the material surrounding the source produces synchrotron emission in the X-ray, optical, and radio wavelengths. This "afterglow" lasts from days to months depending on the frequency range.

Different models have been applied to the observations that followed GW170817. Among the most popular is the classical case of a narrow and highly relativistic jet powered by a compact central engine (Goldstein et al. 2017). Deviations in the light curves derived from classical models have motivated further developments (Willingale et al. 2007; Cannizzo & Gehrels 2009; Metzger et al. 2011; Duffell & MacFadyen 2015), including Gaussian structured jets (Kumar & Granot 2003; Abbott et al. 2017b; Troja et al. 2017) that can be detected off-axis and do not require the jet to point directly to Earth. Other models predict a more isotropic emission profile, produced by an expanding cocoon formed as the jet makes its way through the ejected material, reaching a Lorentz factor on the order of a few (i.e., $\Gamma \sim 2$ to 3; Nagakura et al. 2014; Lazzati et al. 2017; Kasliwal et al. 2017; Mooley et al. 2017).

In addition to the GRB afterglow, in the event of a BNS or NSBH merger, the highly neutron-rich material undergoes rapid neutron capture (*r*-process), which creates heavy elements and enriches galaxies with rare metals (Côté et al. 2018). Some of the products of the *r*-process include radioactive elements; the decay of these newly created elements can energize the ejecta. The produced thermal radiation eventually powers a transient known as a *kilonova* (KN) (Lattimer & Schramm 1974; Li & Paczynski 1998; Metzger et al. 2010; Rosswog 2015; Kasen et al. 2017). In the case of an on-axis SGRB, in most cases the optical emission is expected to be dominated by the afterglow and not by the KN. (Gompertz et al. 2018; Zhu et al. 2021). There have been attempts to separate the light of the SGRB afterglow and the KN (Fong et al. 2016; Ascenzi et al. 2019; Troja et al. 2019; Rossi et al. 2020; Fong et al. 2021; O'Connor et al. 2021), however; this still presents a number of challenges.

Identifying optical counterparts to compact binary mergers can provide a rich scientific output, as demonstrated by the discovery of AT2017gfo (Chornock et al. 2017; Coulter et al. 2017; Cowperthwaite et al. 2017; Drout et al. 2017; Evans et al. 2017; Kasliwal et al. 2017; Kilpatrick et al. 2017; Lipunov et al. 2017; McCully et al. 2017; Nicholl et al. 2017; Pian et al. 2017; Shappee et al. 2017; Smartt et al. 2017), which led to discoveries in areas as diverse as *r*-process nucleosynthesis, jet physics, host galaxy properties, and even cosmology (Arcavi et al. 2017; Chornock et al. 2017; Drout et al. 2017; Kasen et al. 2017; Kasliwal et al. 2017; Pian et al. 2017; Smartt et al. 2017;

Tanvir et al. 2017; Troja et al. 2017). Previous studies have used the arcminute localizations achieved with the Neil Gehrels Swift Observatory Burst Alert Telescope (BAT) to find and characterize SGRBs optical counterparts (Fong et al. 2015; Rastinejad et al. 2021), however the number of associations is still only a few dozen. Others have tried following up thousands of square degrees of LIGO-Virgo Collaboration (LVC) maps (Andreoni et al. 2019, 2020; Coughlin et al. 2019a, 2019b; Goldstein et al. 2019; Hosseinzadeh et al. 2019; Vieira et al. 2020; Anand et al. 2021; Kasliwal et al. 2020) in the hopes of localizing EM counterparts to gravitational-wave events, to no avail. Moreover, other studies have tried to serendipitously find the elusive KN (Chatterjee et al. 2019; Andreoni et al. 2020, 2021), but they have so far only been able to constrain the local rate of neutron star mergers using wide field-of-view (FOV) synoptic surveys.

In this paper, we present a summary of the systematic and dedicated optical search of Fermi-GBM SGRBs using the Palomar 48 inch telescope equipped with the 47 square degree Zwicky Transient Facility camera (Graham et al. 2019; Bellm et al. 2019a) over the course of ∼2 yr. Previous studies (Singer et al. 2013, 2015) have successfully found optical counterparts to GBM LGRBs using the intermediate Palomar Transient Factory (iPTF) (Law et al. 2009; Rau et al. 2009), and other have serendipitously found orphan afterglows and LGRBs using ZTF (Andreoni et al. 2021; Ho et al. 2022). There are ongoing projects like Global MASTER-Net (Lipunov et al. 2005), and the Gravitational-Wave Optical Transient Observe (GOTO; Mong et al. 2021) that are using optical telescopes to scan the large regions derived by GBM. We note that the optical afterglows of LGRBs are usually brighter than those of SGRBs, thus the ToO strategy might differ from the one presented in this paper. We base our triggers on GBM events since GBM is more sensitive to higher energies than Swift and it detects SGRBs at four times the rate of Swift, making it the most prolific compact binary merger detector.

In Section 2, we describe the facilities involved along with the observations and data taken during the campaign. We describe our filtering criteria and how candidates are selected and followed up in Section 3, and detail the Fermi events we followed up in Section 4. In Section 5, we compare our observational limits to SGRB transients in the literature. In Section 6, we discuss the implications of the optical non-detection of a source and we explore the sensitivity of our searches. Using the light curves of the transients generated for our efficiency analysis, we put the detection of an optical counterpart in context for future ToO follow-up efforts in Section 7. We summarize our work in Section 8.

2. Observations and Data

In this section, we will broadly describe the characteristics of the telescopes and instruments involved in this campaign, as well as the observations. We start with the Fermi-GBM, our source of compact mergers, followed by ZTF, our optical transient discovery engine, and finally describe the facilities used for follow-up. The magnitudes are given in the AB system throughout this paper.

2.1. Fermi *Gamma-Ray Burst Monitor*

The Gamma-ray Burst Monitor (GBM) is an instrument on board the Fermi Gamma-ray Space Telescope sensitive to gamma-ray photons with energies from 8 keV to 40 MeV (Meegan et al. 2009). The average rest-frame energy peak for SGRBs ($E_{p,i} \sim 0.5$ MeV; Zhang et al. 2012) is enclosed in the observable GBM energy range and not in the Swift BAT energy range (5–150 keV). Additionally, any given burst should be seen by a number of detectors, as GBM is sensitive to gamma-rays from the entire unocculted sky.

The low local rate of Swift SGRBs has impeded the discovery of more GW170817-like transients (Dichiara et al. 2020). On the other hand, GBM detects close to 40 SGRBs per year (Meegan et al. 2009), four times the rate of Swift. However, the localization regions given by GBM usually span a large portion of the sky, going from a few hundred square degrees to even a few thousand square degrees. These large regions make the systematic search for counterparts technically challenging and time consuming (Goldstein et al. 2020; von Kienlin et al. 2020).

Our adopted strategy prioritizes Fermi-GBM GRB events visible from Palomar that present a hard spike, that are classified as SGRBs by the on-board GBM algorithm, and that are not detected by Swift. During the first half of our campaign (2018), we did not have any constraints on the size of the GRB localization region. However, during the second half of our campaign, we restricted our triggers to the events for which more than 75% of the error region could be covered twice in ∼2 hr. With ZTF this corresponds to a requirement that 75% of the map encloses less than 500 deg^2., which explains the difference in the number of triggers between the first and second half of our campaign.

For each GRB, we calculate the probability of belonging to the population that clusters the SGRBs based on their Comptonized energy peak $E_{\rm peak}$ and their duration T_{90}. For this, we fit two log-normal distributions (representing the long and short classes) to a sample of 2300 GRBs. We derive and color code the probability $P_{\rm SGRB}$ by assessing where each GRB falls in the distribution (see Figure 1, and Ahumada et al. 2021 for more details). In Table 1, we list the relevant features of the SGRBs selected for follow-up.

2.2. *The Zwicky Transient Facility*

We have used ZTF to scan the localization regions derived by the Fermi-GBM. ZTF is a public-private project in the time domain realm that employs a dedicated camera (Dekany et al. 2020) on the Palomar 48 inch Schmidt telescope. The ZTF field of view is 47 deg^2, which usually allows us to observe more than 50% of the SGRB error region in less than one night. The public ZTF survey (Bellm et al. 2019b) covers the observable northern sky every two nights in g and r bands with a standard exposure time of 30 s, reaching an average 5σ detection limit of $r = 20.6$.

Two ToO strategies were tested during this campaign, one during 2018 and the second during 2020–2021. Most modifications came after lessons learned during the follow-up efforts of gravitational waves in 2019 (Coughlin et al. 2019b; Kasliwal et al. 2020; Anand et al. 2021). The original ToO observing plan allowed us to start up to 36 hr from the SGRB GBM trigger. However, since the afterglow we expect is already faint ($m_r > 19$ mag) and fast fading ($\Delta m/\Delta t > 0.3$ mag per day), our revised strategy only includes triggers that can be observed from Palomar within 12 hr. The exposure time for each trigger ranges from 60 s to 300 s, depending on the size of the localization region, as there is a trade-off between exposure

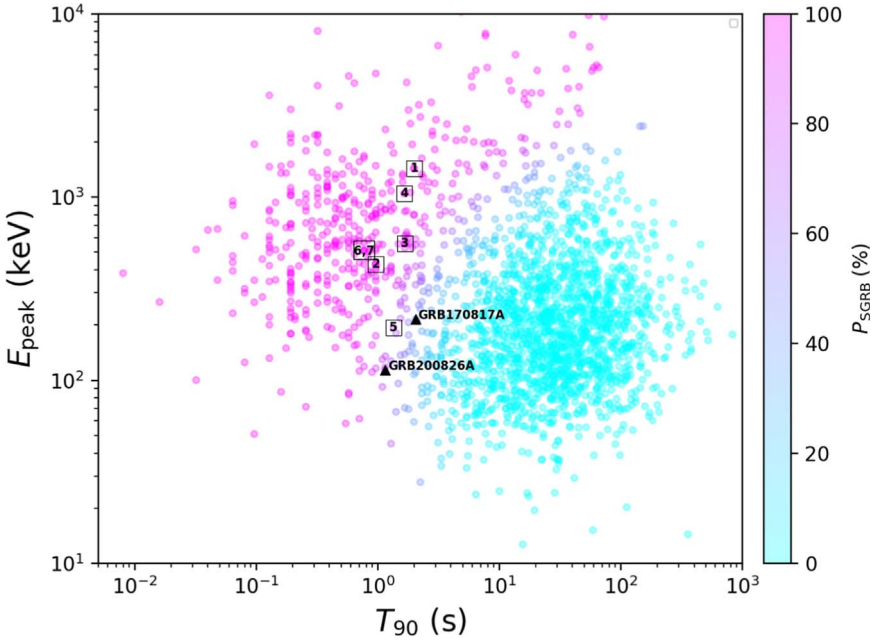

Figure 1. The peak energy based on a Comptonized fit, E_{peak} (keV), vs. the time-integrated T_{90} (s), for 2310 Fermi-GBM GRBs. The data are fit with two log-normal distributions for the two GRB classes. The color of the data points indicates the probability, with magenta being 100% SGRB and cyan being 100% LGRB. We show in squares numbered from 1 to 7 the following SGRBs: GRB 180523B, GRB 180626C, GRB 180715B, GRB 181126B, GRB 210510A, GRB 180913A, and GRB 180728B. Note that the GRB 180728B and GRB 180913A share the same location in this parameter space. The bursts GRB 200514B and GRB 201130A are not shown as the power-law model is preferred over the Comptonized fit, thus there is no E_{peak} parameter associated to them. For context, we show in triangles GRB 170817A and GRB 200826A.

time and coverage. We generally prioritized coverage over depth and, for the second half of our campaign, we only triggered on maps where more than 75% of the region could be covered. The same sequence is repeated a second time the following night, unless additional information from other spacecraft modifies the error region. Generally, fields with an air mass > 2.5 are removed from the observing plan.

We schedule two to three sets of observations depending on the visibility of the region, using the ZTF r and g bands. The combination of r- and g-band observations was motivated by the need to look for afterglows and KNe, which are both fast-evolving red transients. In fact, the SGRB afterglows in the literature show red colors (i.e., $g - r > 0.3$ mag) and a rapid evolution, fading faster than $\Delta m_r/\Delta t > 0.5$ mag per day. On the other hand, GW170817 started off with bluer colors and evolved dramatically fast in the optical during the first days, with $g - r = 0.5$ mag 1 day after the Fermi alert and $\Delta m_g/\Delta t > 1$ mag per day. Even though we expect a fast-fading transient, if we assume conservative fading rates of 0.3-0.5 mag per day, we would need observations separated by 8 to 5 hr, respectively, to detect the decline using ZTF data with photometric errors of the order of 0.1 mag. This ToO strategy thus relies on the color of transients for candidate discrimination, as this is easier to schedule than multi-epoch single-band photometry within the same night and with sufficient spacing between observations.

We followed up on 10 Fermi-GBM SGRBs, and we show nine sky maps and their corresponding ZTF footprints in Figures 2, 3, and 4. Please refer to Ahumada et al. (2021) for details on GRB 200826A, the only short-duration GRB followed up during our campaign that is not shown here. As listed in Table 1, all of the events span more than 100 deg^2, which is the average localization region covered during previous LGRBs searches (Singer et al. 2015). Moreover, in many cases, the 90% credible region (C.R.) spans more than 1000 deg^2, which is challenging even for a 47 deg^2 field-of-view instrument such as ZTF.

Triggering ToO observations for survey instruments like ZTF and Palomar Gattini-IR (De et al. 2020) halts their ongoing survey observations and redirects them to observe only certain fields as directed by an observation plan. We have used `gwemopt` (Coughlin et al. 2018, 2019c), a code intended to optimize targeted observations for gravitational-wave events, to achieve an efficient schedule for our ToO observations. The similarities between LVC and GBM skymaps allow us to apply the same algorithm, which involves slicing the skymap into the predefined ZTF tiles and determining the optimal schedule by taking into consideration the observability windows and the need for a repeated exposure of the fields. In order to prioritize the fields with the highest enclosed probability, we used the "greedy" algorithm described in Coughlin et al. (2018) and Almualla et al. (2020). As `gwemopt` handles both synoptic and galaxy-targeted search strategies, we employed the former to conduct observations with some of our facilities, Palomar Gattini-IR, GROWTH-India and ZTF, and the latter for scheduling observations with the Kitt Peak EMCCD Demonstrator (KPED; Coughlin et al. 2019b).

2.3. Optical Follow-up

Following the identification of candidate counterparts with ZTF, subsequent optical follow-up of these transients is required to characterize and classify them. For the candidates that met the requirements described in Section 3, mainly that they showed interesting light-curve history and magnitude evolution, we acquired additional data. To obtain these data, the GROWTH multi-messenger group relies on a number of telescopes around the globe. Most of these facilities are strategically located in the Northern Hemisphere, enabling

Table 1
Global Features of the Fermi-GBM SGRB Followed Up with ZTF

GRB	Fermi Trigger	Time [JD]	T_{90} [s]	90% (50%) C.R. [deg^2]	S/N	$E_{\rm peak}$ [keV]	Fluence [10^{-8} erg cm^{-2}]	$P_{\rm SGRB}$
GRB 180523B	548793993	2458262.2823	2.0 ± 1.4	5094 (852)	6.9	1434 ± 443	25.7 ± 2.3	0.99
GRB 180626C	551697835	2458295.8916	1.0 ± 0.4	5509 (349)	7.1	431 ± 81	49.1 ± 3.8	0.97
GRB 180715B	553369644	2458315.2412	1.7 ± 1.4	4383 (192)	12.5	560 ± 89	52.0 ± 1.7	0.92
GRB 180728B	554505003	2458328.3819	0.8 ± 0.6	397 (47)	20.2	504 ± 61	130.9 ± 2.0	0.99
GRB 180913A	558557292	2458375.2834	0.8 ± 0.1	3951 (216)	10.0	508 ± 90	79.1 ± 2.0	0.99
GRB 181126B	564897175	2458448.6617	1.7 ± 0.5	3785 (356)	7.5	1049 ± 241	48.3 ± 3.2	0.99
GRB 200514B	611140062	2458983.8802	1.7 ± 0.6	590 (173)	5.1	†	17.8 ± 1.1	—
GRB 201130A	628407054	2459183.7297	1.3 ± 0.8	545 (139)	5.3	†	37.0 ± 5.2	—
GRB 210510A	642367205	2459345.3055	1.3 ± 0.8	1170 (343)	5.6	194 ± 60	23.2 ± 1.4	0.74
GRB 200826A	620108997	2459087.6874	1.1 ± 0.1	339 (63)	8.1	88.9 ± 3.2	426.5 ± 2.2	0.74

Note. The peak energies come from the public Fermi catalog (von Kienlin et al. 2020) for GRB 180523B, GRB 180626C, GRB 180715B, GRB 180913A, and GRB 181126B. Additionally, we compiled E_p listed in Hamburg et al. (2018) for GRB 180728B, and independently provide time-integrated fits for GRB 200514B, GRB 201130A, and GRB 210510A over the T_{90}. We list the GRB name, their trigger number, the Julian day (JD) of each event, the T_{90} duration, the area encompassed by the 90% (50%) credible region (C.R.), the signal-to-noise ratio from the Fermi detection, the peak energy of the gamma-ray spectrum ($E_{\rm peak}$), the fluence of the burst, and the probability of the burst to belong to the SGRB population (see Section 2.1). The area associated with a given C.R. is derived by calculating the number of pixels that cumulatively sum a specific percentage, using the HEALPix map of each GRB. For events with a †, the power-law model is preferred over the Comptonized model, thus there is no E_p parameter. We show separately the parameters of GRB 200826A, as it was not related to a compact binary merger (Ahumada et al. 2021).

continuous follow-up of ZTF sources. The follow-up observations included both photometric and spectroscopic observations. Even though the spectroscopic classification is preferable, photometry was essential to rule out transients, based on their color evolution and fading rates. The telescopes involved in the photometric and spectroscopic monitoring are briefly described in the following paragraphs.

We used the Kitt Peak Electron multiplying CCD Demonstrator (KPED) on the Kitt Peak 84 inch telescope (Coughlin et al. 2019b) to obtain photometric data. The KPED is an instrument mounted on a fully robotic telescope and it has been used as a single-band optical detector in the Sloan g and r bands and Johnson UVRI filters. The FOV is $4\farcm4 \times 4\farcm4$ and the pixel size is $0\farcs259$.

Each candidate scheduled for photometry was observed in the g and r band for 300 s. The data taken with KPED are then dark subtracted and flat-field calibrated. After applying astrometric corrections, the instrumental magnitudes were determined using Source Extractor (Bertin & Arnouts 1996). To calculate the apparent magnitude of the candidate, the zero-point of the field is calibrated using Pan-STARRS 1 (PS1) and Sloan Digital Sky Survey (SDSS) stars in the field as standards. Given the coordinates of the target, an on-the-fly query to PAN-STARRS 1 and SDSS retrieves the stars within the field that have a minimum of four detections in each band.

Additionally, sources were photometrically followed up using the Las Cumbres Observatory Global Telescope (LCOGT) (PI: Coughlin, Andreoni) (Brown et al. 2013). We used the 1 m and 2 m telescopes to schedule sets of 300 s in the g, r, and i bands. The LCOGT data come already processed and, in order to determine the magnitude of the transient, the same PS1/SDSS cross-matching strategy used for KPED was implemented for LCOGT images.

We used the Spectral Energy Distribution Machine (SEDM) on the Palomar 60 inch telescope (Blagorodnova et al. 2018) to acquire g-, r-, and i-band imaging with the Rainbow Camera on SEDM in 300 s exposures. Images were then processed using a python-based pipeline that performs standard photometric reduction techniques and uses an adaptation of `FPipe` (Fremling Automated Pipeline; described in detail in Fremling et al. 2016) for difference imaging. Moreover, we employed the Integral Field Unit (IFU) on SEDM to observe targets brighter than $m_{AB} < 19$ mag. Each observation is reduced and calibrated using the `pysedm` pipeline (Rigault et al. 2019), which applies standard calibrations using standards taken during the observing night. Once the spectra are extracted we use the `SuperNova IDentification`[42] software (`SNID`; Blondin & Tonry 2007) for spectroscopic classification.

We obtained spectra for six candidates using the Double Spectrograph (DBSP) on the Palomar 200 inch telescope during classical observing runs. The data were taken using the $1.5''$ slit and reduced following a custom PyRAF pipeline[43] (Bellm & Sesar 2016).

The other telescopes used for photometric follow-up are the GROWTH India telescope (GIT) in Hanle, India, the Liverpool Telescope (Steele et al. 2004) in La Palma, Spain, and the Akeno telescope (Kotani et al. 2005) in Japan. The requested observations in the g, r, and i band varied between 300 s and 600 s depending on the telescope.

We obtained spectra with the DeVeny Spectrograph at the Lowell Discovery Telescope (LDT) (MacFarlane & Dunham 2004) and the 10 m Keck Low Resolution Imaging Spectrograph (LRIS) (Oke et al. 1995). We reduced these spectra with PyRAF following standard long-slit reduction methods.

We used the Gemini Multi-Object Spectrograph (GMOS-N) mounted on the Gemini North 8 m telescope on Maunakea to obtain photometric and spectroscopic data (P.I. Ahumada, GN-2021A-Q-102). Our standard photometric epochs consisted of four 180 s exposures in the r band to measure the fading rate of the candidates, although we included the g band when the color was relevant. These images were processed using DRAGONS (Labrie et al. 2019) and the magnitudes were derived after calibrating against PS1. When necessary and possible, we used PS1 references to subtract the host, using HOTPANTS. For spectroscopic data, our standard was four 650 s exposures

[42] https://people.lam.fr/blondin.stephane/software/SNID/
[43] https://github.com/ebellm/pyraf-dbsp

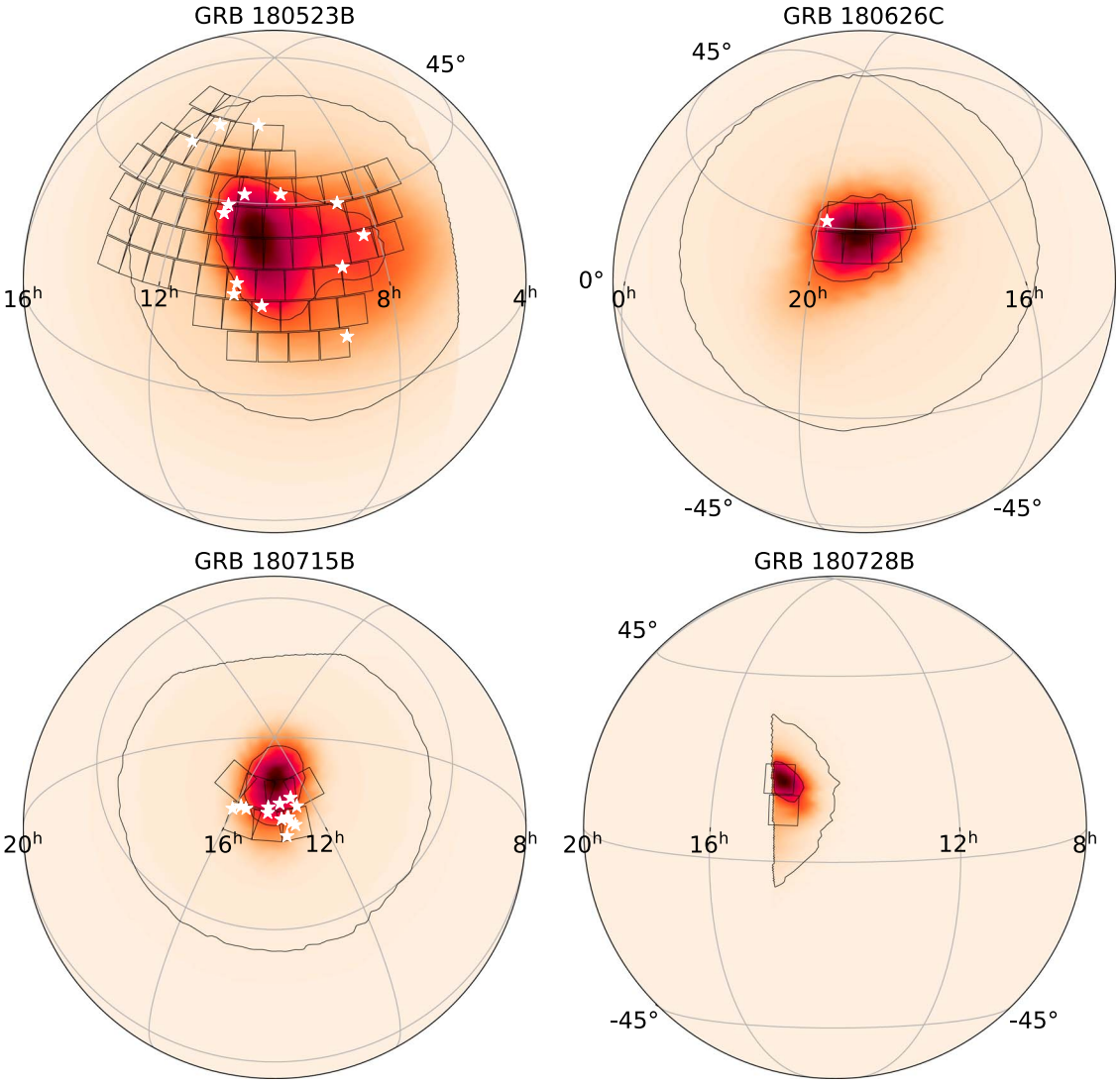

Figure 2. Coverage of four ZTF triggers and their Fermi-GBM localization regions. Starting on the top left, the sky maps of GRB 180523, GRB 180626, GRB 180715, and GRB 180728 are shown along the ≈47 deg^2 ZTF tiles (black quadrilaterals). The 50% and 90% credible regions are shown as black contours and the sources discovered during the ZTF trigger as white stars (details in Section 4). The grid shows the R.A. in hours and the decl. in degrees.

using the 1″ long-slit and the R400 grating and we used PyRAF standard reduction techniques to reduce the data.

3. Candidates

After a given ZTF observation finishes, the resulting image is subtracted to a reference image of the field (Masci et al. 2019; Zackay et al. 2016). The latter process involves a refined PSF adjustment and a precise image alignment in order to perform the subtraction and determine flux residuals. Any 5σ difference in brightness creates an "*alert*" (Patterson et al. 2019), a package with information describing the transient. The alerts include the magnitude of the transient, proximity to other sources, and its previous history of detections among other features. ZTF generates around 10^5 alerts per night of observation, which corresponds to $\sim 10\%$ of the estimated Vera Rubin observatory alert rate. The procedure to reduce the number of alerts from $\sim 10^5$ to a handful of potential optical SGRB counterparts is described in this section.

In general terms, the method involves a rigid online alert filtering scheme that significantly reduces the number of sources based on image quality features. Then, the selection of candidates takes into consideration the physical properties of the transient (i.e., cross-matching with AGN and solar system objects), as well as archival observations from different surveys. After visually inspecting the candidates that passed the preliminary filters, scientists in the collaboration proceed to select sources based on their light curves, color, and other features (i.e., proximity to a potential host, redshift of the host, etc.). This method allows us to recover objects that are later scheduled for further follow-up.

The candidate selection and the follow-up are coordinated via the GROWTH marshal (Kasliwal et al. 2019) and lately through the open-source platform and alert broker Fritz.[44]

3.1. Detection and Filtering

In the searches for the optical counterpart for SGRBs, we query the ZTF data stream using the GROWTH marshal (Kasliwal et al. 2019), the `Kowalski` infrastructure (Duev et al. 2019)[45] , the `NuZTF` pipeline (Stein et al. 2021, 2021) built

[44] https://github.com/fritz-marshal/fritz
[45] https://github.com/dmitryduev/kowalski

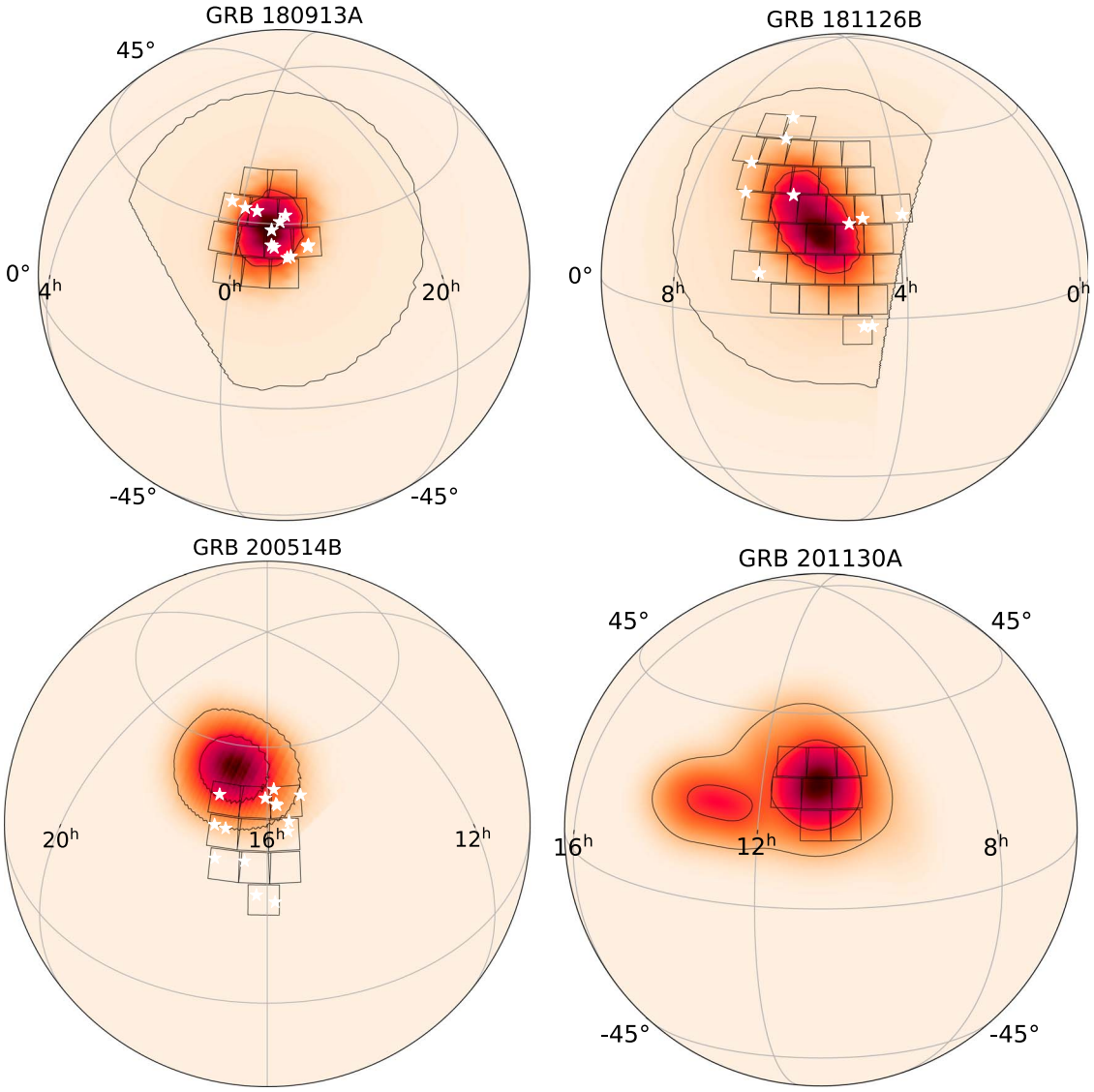

Figure 3. Coverage of four ZTF triggers and their Fermi-GBM localization regions. From top to bottom and left to right, the sky maps of GRB 180913, GRB 181126, GRB 200514, and GRB 201130 are shown along the ≈47 deg^2 ZTF tiles (black quadrilaterals). The 50% and 90% credible regions are shown as black contours and the sources discovered during the ZTF trigger as white stars (details in Section 4). Note that, for GRB 200514, we tiled the preliminary region, which was offset from the final localization. The grid shows the R.A. in hours and the decl. in degrees.

using `Ampel`(Nordin et al. 2019)[46] , and Fritz. The filtering scheme restricted the transients to those with the following properties:

1. *Within the sky map:* To ensure the candidates are in the GBM skymap, we implemented a cone search in the GBM region with `Kowalski` and `Ampel`. With the GROWTH marshal approach, we retrieve only the candidates in the fields scheduled for ToO. We note that a more refined analysis on the coordinates of the candidates is done after this automatic selection.
2. *Positive subtraction:* After the new image is subtracted, we filter on the sources with a positive residual, thus the ones that have brightened.
3. *It is real:* To distinguish sources that are created by ghosts or artifacts in the CCDs, we apply a random-forest model (Mahabal et al. 2019) that was trained with common artifacts found in the ZTF images. We restrict the real-bogus score to > 0.25, as it best separates the two populations. For observations that occurred after 2019, we used the improved deep-learning real-bogus score `drb` and we set the threshold to sources with `drb` score > 0.15 (Duev et al. 2019).
4. *No point source underneath:* To rule out stellar variability, we require the transient to have a separation of 3″ from any point source in the PS1 catalog based on Tachibana & Miller 2018.
5. *Two detections:* We require a minimum of two detections separated by at least 30 minutes. This allows us to reject cosmic rays and moving solar system objects.
6. *Far from a bright star:* To further avoid ghosts and artifacts, we require the transient to be $> 20''$ from any bright ($m_{\rm AB} < 15$ mag) star.
7. *No previous history:* As we do not expect the optical counterpart of a SGRB to be a periodic variable source, we restrict our selection to only sources that are detected after the event time and have no alerts generated for dates prior to the GRB.

[46] https://github.com/AmpelProject

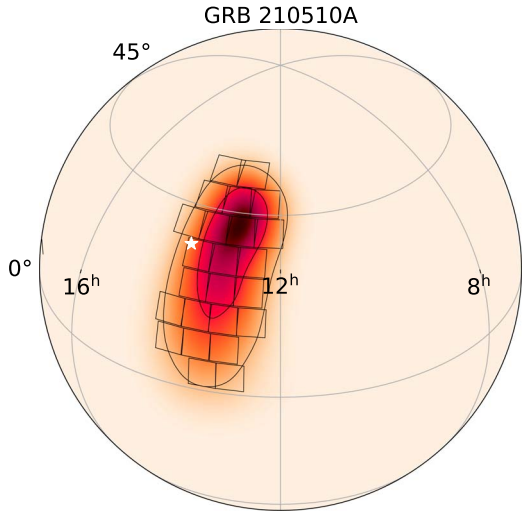

Figure 4. Coverage of the ZTF trigger and Fermi-GBM localization region of GRB 210510, along the ≈47 deg^2 ZTF tiles (black quadrilaterals). The 50% and 90% credible regions are shown as black contours and the source discovered during the ZTF trigger as white star (details in Section 4). The grid shows the R.A. in hours and the decl. in degrees.

As a reference, this first filtering step reduced the total number of sources to a median of ∼0.03% of the original number of alerts. The breakdown of each filter step is shown in Table 2. A summary of the numbers of followed-up objects for each trigger is in Table 3 and the details of the filtering scheme are described below. More than 3×10^5 alerts were generated during the nine ToO triggers, while ∼80 objects were circulated in the Gamma-ray Coordinates Network (GCN).

3.2. Scanning and Selection

Generally, after the first filter step, the number of transients is reduced to a manageable amount ∼ $O(100)$. These candidates are then cross-matched with public all-sky surveys such as Wide-field Infrared Survey Explorer (WISE; Cutri et al. 2013), Pan-STARRS 1 (PS1; Chambers et al. 2016), Sloan Digital Sky Survey (SDSS; Ahumada et al. 2020a), the Catalina Real-time Transient Survey (CRTS; Drake et al. 2009), and the Asteroid Terrestrial-impact Last Alert System (ATLAS; Tonry 2011). We use the WISE colors to rule out candidates, as active galactic nuclei (AGN) are located in a particular region in the WISE color space (Wright et al. 2010; Stern et al. 2012). If a candidate has a previous detection in ATLAS or has been reported to the Transient Name Server (TNS) before the event time, it is also removed from the candidate list. We additionally cross-match the position of the candidates with the Minor Planet Center (MPC) to rule out any other slow-moving object. We use the PS1 DR2[47] to query single detections at the location of the transients, and we use this information to rule out sources based on serendipitous previous activity.

One of the most important steps in our selection of transients is the rejection of sources using forced photometry (FP) on ZTF images. For this purpose, we run two FP pipelines: ForcePhotZTF[48] (Yao et al. 2019) and the ZTF FP pipeline (Masci et al. 2019). We limit our search to 100 days before the burst and reject sources with consistent $\geqslant 4\sigma$ detections.

Finally, we manually scan and vet candidates passing those cuts, referring to cutouts of the science images, photometric decay rates, and color evolution information in order to select the most promising candidates (see Figure 5).

Detailed tables with the candidates discovered by ZTF for the SGRB campaign are shown in Table 4.

3.3. Rejection Criteria

In order to find an optical counterpart, further monitoring of the discovered transients is needed. We have taken spectra for the most promising candidates to classify them. Most of the spectra acquired correspond to bright SNe (as in Figure 6) and a few cataclysmic variables (CVs) and an AGN. After the nine SGRB follow-ups, we obtained 19 spectra, however none of them exhibited KN features. We have used the "Deep Learning for the Automated Spectral Classification of Supernovae and Their Hosts" or `dash` (Muthukrishna et al. 2019) to determine the classification of the candidates with SN spectral features. CVs were recognized as they show H features at redshift $z = 0$.

For the sources that do not have spectra available, we monitored their photometric evolution with the facilities described in Section 2. Even though the photometric classification cannot be entirely conclusive, there are characteristic features shared between afterglows and KNe. On one side, afterglows are known to follow a power-law decay of the form $F \sim t^{-\alpha}$. On the other hand, most KN models (Bulla 2019) show evolution faster than 0.3 mag per day (Andreoni et al. 2020; Anand et al. 2021). As a reference, GW170817 faded over ∼1 mag over the course of 3 days and other SGRB optical counterparts have shown a rapid magnitude evolution as well (Fong et al. 2015; Rastinejad et al. 2021). The astrophysical events that most contaminated our sample are SNe, but they normally show a monotonic increase in their brightness during their first tens of days, to later decline at a slower rate than expected for afterglows or KNe. Other objects like slow-moving asteroids and flares are less common and can be removed inspecting the images or performing a detailed archival search in ZTF and other surveys.

To illustrate the photometric rejection, we show two transients in Figure 5 with no previous activity in the ZTF archives previous to the SGRB. As their magnitude evolution in both the r and g band does not pass our threshold, we conclude that they are not related to the event. This process was repeated for all candidates without spectral information, using all the available photometric data from ZTF and partner telescopes.

4. SGRB Events

4.1. GRB 180523B

The first set of ToO observations of this program was taken 9.1 hr after GRB 180523B (trigger 548793993). We covered ∼2900 deg^2, which corresponds to 60% of the localization region after accounting for chip gaps in the instrument (Coughlin et al. 2018b). The median 5σ upper limit for an isolated point source in our images was $r > 20.3$ mag and $g > 20.6$ mag and after 2 days of observations we arrived at 14 viable candidates that required follow-up. We were able to spectroscopically classify four transients as SNe and photometrically follow up sources with KPED to determine that the magnitude evolution was slower than our threshold. This effort was summarized in Coughlin et al. (2019a) and the list of transients discovered is displayed in Table 4.

[47] https://catalogs.mast.stsci.edu/panstarrs/
[48] https://github.com/yaoyuhan/ForcePhotZTF

Table 2
Summary of the Efficiency of our Vetting Strategy

GRB	SNR > 5	Positive Subtraction	Real	Not Star Underneath	Far From Bright Star	Two Detections	Circulated in GCNs
GRB 180523B	67614	17374	12117	687	669	297	14
GRB 180626C	10602	5040	4967	1582	1377	214	1
GRB 180715B	33064	7611	7515	6941	5509	104	14
GRB 180728B	18488	1450	1428	859	739	51	7
GRB 180913A	25913	12105	12077	6284	5145	372	12
GRB 181126B	40342	30455	30416	22759	21769	340	11
GRB 200514B	20610	10983	10602	4502	4422	1346	14
GRB 200826A	13488	8142	7744	3892	3785	464	14
GRB 201130A	1972	1045	990	647	637	43	0
GRB 210510A	41683	27229	28940	16977	16973	1562	1
Median reduction		50.27%	48.53%	23.05 %	20.66%	1.73%	0.03%

Note. For each GRB, we list the number of alerts that survives after a given filtering step. The first column (SNR > 5) shows the total number of alerts in the GRB map. The next column displays the number of alerts that show an increase in flux (Positive Subtraction). The Real column shows the number of sources considered as real using either the real-bogus index (RB) or `drb` scores. We set the thresholds to RB > 0.25 and `drb` > 0.5. The next columns show the number of sources that are not related to a point source, nor close to a bright star, to avoid artifacts. To avoid moving objects, we show the number of sources with two detections separated by at least 30 minutes. The last column shows the number of sources we circulated as potential candidates for each trigger. For each step, we calculate the median reduction of alerts and list this number at the end of each column.

4.2. GRB 180626C

The SGRB GRB 180626C (Fermi trigger 551697835) came in the middle of the night at Palomar. We started observing after 1.5 hr and were able to cover 275 deg^2 of the GBM region. The localization, and hence the observing plan, was later updated as the region of interest was now the overlap between the Fermi and the newly arrived InterPlanetary Network (IPN)[49] map. The observations covered finally 230 deg^2, corresponding to 87% of the intersecting region. After two nights of observations, with a median 5σ upper limit of $r >$ 20.9 mag and $g > 21.0$ mag, only one candidate was found to have no previous history of evolution and be spatially coincident with the SGRB (Coughlin et al. 2018a).

The transient ZTF18aauebur was a rapidly evolving transient that faded from $g = 18.4$ to $g = 20.5$ in 1.92 days. This rapid evolution continued during the following months, fluctuating between $r \sim 18$ mag and $r \sim 19$ mag. It was interpreted as a stellar flare, as it is located close to the Galactic plane and there is an underlying source in the PS1 and GALEX (Morrissey et al. 2007) archive. Additionally, its SEDM spectrum showed a featureless blue spectrum and Hα absorption features at redshift $z = 0$, so it is an unrelated Galactic source (see Table 4) .

4.3. GRB 180715B

We triggered ToO observations to follow up GRB 180715B (trigger 553369644) 10.3 hr after the GBM detection. We managed to observe ∼37% of the localization region which translates into 254 deg^2. The median limiting magnitude for these observations was $r > 21.4$ mag and $g > 21.3$ mag.

During this campaign, we discovered 14 new transients (Cenko et al. 2018) in the region of interest. We were able to spectroscopically classify two candidates using instruments at the Palomar 60 inch telescope (P60) and Palomar 200 inch Hale telescope (P200). The SEDM spectrum of ZTF18aauhpyb showed a stellar source with Balmer features at redshift $z = 0$ and a blue continuum. The DBSP spectrum of ZTF18abhbfqf was best fitted by an SN Ia-91T. We show the rejection criteria used to rule out associations with the SGRB in Table 4. Generally, most candidates showed a slow magnitude evolution. Furthermore, three candidates (ZTF18abhhjyd, ZTF18abhbfoi, and ZTF18abhawjn) matched with an AGN in the Milliquas (Flesch 2019) catalog. A summary of the candidates can be found in Table 4.

[49] http://www.ssl.berkeley.edu/ipn3/index.html

4.4. GRB 180728B

The ToO observations of GRB 180728B (trigger 554505003) started ∼8 hr after the Fermi alert, however, it did not cover the later updated IPN localization. The following night and 31 hr after the Fermi detection, we managed to observe the joint GBM and IPN localization, covering 334 deg^2 which is ∼76% of the error region. The median upper limits for the scheduled observations were $r > 18.7$ mag and g > 20.0 mag (Coughlin et al. 2018a). As a result of these observations, no new transients were found.

4.5. GRB 180913A

We triggered ToO observations with ZTF to follow up the Fermi event GRB 180913A (trigger 558557292) about ∼8 hr after the GBM detection. The first night of observations covered 546 deg^2. The schedule was adjusted as the localization improved once the IPN map was available. During the second night, we covered 53% of the localization, translated into 403 deg^2. After a third night of observations, 12 transients were discovered and circulated in Coughlin et al. 2018b. The median upper limits for this set of observations were $r >$22.2 mag and $g > 22.1$ mag.

We obtained a spectrum of ZTF18abvzfgy with LDT, a fast-rising transient ($\Delta m/\Delta t \sim -0.2$ mag per day) in the outskirts of a potential host galaxy. It was classified as an SN Ic at a redshift of $z = 0.04$. The rest of the transients were followed up photometrically with KPED and LCO, but generally showed a flat evolution. The candidate ZTF18abvzsld had previous PS1 detections, thus ruling it out as a SGRB counterpart. The rest of the candidates are listed in Table 4.

Table 3
Summary of the ZTF ToO Triggers

GRB	Area Covered	C.R. Covered	Time Difference T_b $T_{ZTF,s}$ and $T_{ZTF,e}$	Exposure Time (sequence)	r-band 5σ Limit	Objects Followed Up
GRB 180523B	2900 deg^2	60%	9.1 hr—35.9 hr	60 s(rgr), 90 s(rgr)	r > 20.3 mag	14
GRB 180626C	275 deg^2	87%	1.5 hr—22.0 hr	120 s(rgr), 240 s(grg)	r > 20.9 mag	1
GRB 180715B	254 deg^2	37%	10.3 hr—35.5 hr	180 s(rgr), 240 s(rg)	r > 21.4 mag	14
GRB 180728B	334 deg^2	76%	31 hr—32.0 hr	180 s(rgr), 180 s(rgr)	r > 18.7 mag	7
GRB 180913A	403 deg^2	53%	8.3 hr—39.0 hr	180 s(grg), 300 s(grg)	r > 22.2 mag	12
GRB 181126B	1400 deg^2	66%	1.3 hr—27.6 hr	180 s(rr), 300 s (r)	r > 20.5 mag	11
GRB 200514B	519 deg^2	49%	0.9 hr—26.4 hr	300 s(gr)	r > 22.2 mag	14
GRB 201130A	400 deg^2	75%	7 hr—27.9 hr	300 s(grg),300 s(gr)	r > 20.3 mag	0
GRB 210510A	1105 deg^2	84%	10 hr—35.3 hr	180(gr),240(r)	r > 22.1 mag	1

Note. We list the area covered with ZTF, as well as the corresponding credible region (C.R.) of the GBM map. We show the time difference between the burst (T_b) and the start of the ZTF observations ($T_{ZTF,s}$), as well as the time difference between the burst (T_b) and the very last field of the mosaic $T_{ZTF,e}$. For each trigger, we list the exposure time for night 1 and night 2, along with the filter sequence in parenthesis. The last two columns show the median r-band 5σ limit and the number of objects followed up with other facilities.

4.6. GRB 181126B

The last SGRB we followed up before the start of the 2019 O3 LIGO/Virgo observing run was of the Fermi-GBM event GRB 181126B (trigger 564897175). As this event came during the night at the ZTF site, the observations started ∼1.3 hr after the Fermi alert, and we were able to cover 1400 deg^2, close to 66% of the GBM localization. After the IPN localization was available the next day, the observations were adjusted and we used ZTF to cover 709 deg^2, or ∼76% of the overlapped region. The mean limiting magnitude of the observations was r > 20.5 mag (Ahumada et al. 2018). After processing the data, we discovered 11 new optical transients timely and spatially coincident with the SGRB event. We took spectra of seven of them with the Keck LRIS, discovering sox SNe (ZTF18acrkkpc, ZTF18aadwfrc, ZTF18acrfond, ZTF18acrfymv, ZTF18acptgzz, ZTF18acrewzd) and one stellar flare (ZTF18acrkcxa). All of the candidates are listed in Table 4, and none of them showed rapid evolution.

4.7. GRB 200514B

We resumed the search for SGRB counterparts with ZTF once LIGO/Virgo finished O3. On 2020 May 14, we used ZTF to cover over 519.3 deg^2 of the error region of GRB 200514B (trigger 611140062). This corresponds to ∼49% of the error region. After the first night of observations, seven candidates passed our filters and were later circulated in Ahumada et al. (2020). The observations during the following night resulted in seven additional candidates (Reusch et al. 2020a). The depth of these observations reached 22.4 and 22.2 mag in the g and r bands, respectively. After IPN released their analysis (Svinkin et al. 2020), nine of our candidates remained in the localization region. Our follow-up with ZTF and LCO showed that none of these transients evolved as fast as expected for a GRB afterglow (see Table 4).

4.8. GRB 200826A

This burst is discussed extensively in Ahumada et al. (2021), as well as in other works (Rhodes et al. 2021; Rossi et al. 2021; Zhang et al. 2021). It was the only short-duration GRB in our campaign with an optical counterpart association. However, despite its short duration (T_{90}=1.13 s), it showed a photometric bump in the i band that could only be explained by an underlying SN (Ahumada et al. 2020b). This makes GRB 200826A the shortest-duration LGRB (Ahumada et al. 2021).

4.9. GRB 201130A

The ZTF trigger on GRB 201130A reached a depth of $r = 20.3$ mag in the first night of observations after covering 75% of the credible region. No optical transient passed all our filtering criteria (Reusch et al. 2020b).

4.10. GRB 210510A

We triggered optical observations on GRB 210510A (trigger 642367205) roughly 10 hr after the burst. The second night of observations helped with vetting candidates based on their photometric evolution, at least a 0.3 mag per day decay rate is expected for afterglows and KNe. The only candidate that passed our filtering criteria was ZTF21abaytuk (Anand et al. 2021), however its Keck LRIS spectrum showed Hβ, [O II], and [O III] emission features and Mg II absorption lines at redshift of $z = 0.89$ (see Table 4 and Figure 6). Its spectrum, summed with its WISE colors, are consistent with an AGN origin.

5. ZTF Upper Limits

It is possible to compare the search sensitivity, both in terms of depth and timescale, to the expected afterglow and kilonova light curves. In the left panel of Figure 7, the median limits for ZTF observations are shown with respect to known Swift SGRB afterglows with measured redshift from Fong et al. (2015). The yellow light curve corresponds to GW170817 (Abbott et al. 2017c) and the red line is the same GW170817 light curve scaled to a distance of 200 Mpc (see below). Along with GW170817, we show a collection of KN light curves from a BNS grid (Bulla 2019; Dietrich et al. 2020) scaled to 200 Mpc. The regions of the light-curve space explored by each ZTF trigger are represented as gray rectangles and the more opaque region corresponds to their intersection. Even though ZTF has the ability to detect a GW170817-like event and most of the KN light curves, most of the SGRB afterglows observed in the past are below the median sensitivity of the telescope. On the other hand, the counterpart of the GRB 200826A would have been detected in six of our searches, even though it is on the less-energetic part of the LGRB distribution. When scaled

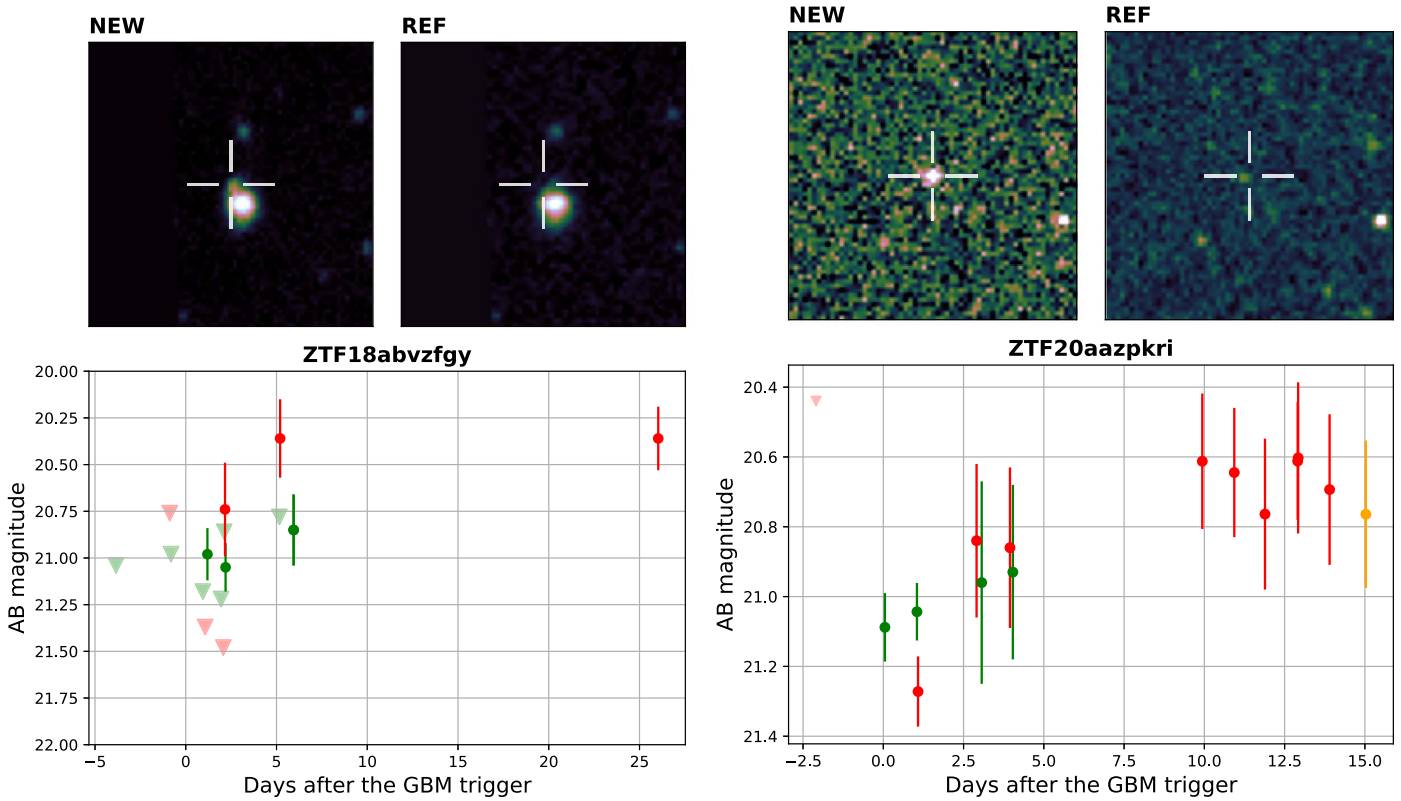

Figure 5. Examples of light curves and cutouts for candidates that passed our filtering criteria. Candidate ZTF18abvzfgy (candidate counterpart to GRB 180913A) in the left panel and ZTF20aazpkri (candidate counterpart to GRB 200514B) in the right panel. The observations in the g and r bands are plotted in green and red colors, respectively. Filled circles represent ZTF detections, while the 5σ upper limits are shown as triangles in the light curve. The top half of each panel shows the discovery image on the left and the reference image on the right. In the 0.7 arcmin^2 cutouts, north is up and east is to the left. A cross marks the location of the transient.

to 200 Mpc, the GW170817 light curve overlaps with the region of five of our searches, suggesting that the combination of depth and rapid coverage of the regions could allow us to detect a GW170817-like event. The searches that do not overlap with the scaled GW170817 have either fainter median magnitude upper limits (<20 mag) or late starting times (>1 day).

We used the redshifts of the SGRBs optical counterparts to determine their absolute magnitudes, which is plotted in the right panel in Figure 7, along with GRB 200826A and GW170817. In order to compare with the ZTF searches and constrain the observations, the median ZTF limits were scaled to a fiducial distance of 200 Mpc, the O3 LIGO/Virgo detection horizon (Abbott et al. 2018) for binary neutron star (BNS) mergers. The range of 200 Mpc is coincidentally approximately the furthest distance at which ZTF can detect a GW170817-like event based on the median limiting magnitudes of this experiment. Moreover, the ZTF region covers most of the KNe models (blue-shaded region) scaled to 200 Mpc. In contrast to the left panel in Figure 7, most of the SGRB optical afterglows fall in the region explored by ZTF. Therefore, if any similar events happened within 200 Mpc, the current ZTF ToO depth plus a rapid trigger of the observations should suffice to ensure coverage in the light-curve space. Previous studies (Dichiara et al. 2020) have come to the conclusion that the low rate of local SGRB is responsible for the lack of detection of GW170817-like transients. In fact, the probability that one of the SGRBs in our sample is within 200 Mpc is 0.3, given the rate derived in Dichiara et al. (2020) of 1.3 SGRB within 200 Mpc per year, assuming an average of 40 SGRBs per year. In Figure 8, we show the same SGRB absolute magnitude light curves but, in this case, we compared them to the ZTF limits scaled to the median redshift of $z=0.47$ from Fong et al. (2015). The ZTF search is still sensitive to SGRB afterglows at these distances within the first day after the GRB event.

6. Efficiency and Joint Probability of Non-detection

In this section, we determine the empirical detection efficiency for each of our searches, and use these efficiencies to calculate the likelihood of detecting an SGRB afterglow in our ToO campaign. With this approach, we are able to set limits on the ZTF's ability to detect SGRB afterglows as a function of the redshift of the SGRB. To accomplish this, we take each GRB we followed up and inject afterglow light curves in the GRB maps at different redshifts. We derive efficiencies using the ZTF observing logs, since these logs contain the coordinates of each successful ZTF pointing and the limiting magnitude of each exposure. This already takes into consideration weather and other technical problems with the survey. In this section, we describe the computational tools used in this endeavor and the results derived from these simulations.

We use `simsurvey` (Feindt et al. 2019) to inject afterglow-like light curves into the GBM skymaps. We distributed the afterglows according to the GBM probability maps and within the 90% credible region of each sky map. We slice the volume into seven equal redshift bins, from $z=0.01$ to $z=2.1$, and injected 7000 sources in each slice. For each injected transient, `simsurvey` employs light-curve models to derive the

Table 4

Follow-up Table of the Candidates Identified for GRB 180523B (Coughlin et al. 2018b), GRB 180626C (Coughlin et al. 2018a), GRB 180715B (Cenko et al. 2018), GRB 180913A (Coughlin et al. 2018b), GRB 181126B (Ahumada et al. 2018), GRB 200514B (Ahumada et al. 2020; Reusch et al. 2020a), and GRB 210510A (Anand et al. 2021)

GRB Trigger	ZTF Name	R.A.	Decl.	Discovery Magnitude	Redshift	Rejection Criteria
GRB 180523B	ZTF18aawozzj	12:31:09.0	+57:35:01.8	$g = 20.20$	(s) 0.095	SN Ia-91T P200
	ZTF18aawnbgg	10:40:54.0	+23:44:43.3	$r = 19.80$	(s) 0.135	SN Ia P200
	ZTF18aawmvbj	10:12:41.1	+21:24:55.5	$r = 19.75$	(s) 0.14	SN Ia P200
	ZTF18aawcwsx	10:40:33.4	+47:02:24.4	$r = 19.84$	(s) 0.09	SN Ia-91T P60
	ZTF18aawnbkw	10:38:47.6	+26:18:51.8	$r = 19.91$	(p) 0.31	Slow SDSS
	ZTF18aawmqwo	09:52:06.9	+47:18:34.8	$r = 19.98$	(p) 0.04	Slow SDSS
	ZTF18aawmkik	08:51:11.4	+13:13:16.7	$r = 19.04$	(p) 0.52	Slow SDSS
	ZTF18aawnmlm	11:03:11.3	+42:07:29.9	$r = 20.12$	Orphan	Slow flat in 7 days
	ZTF18aauhzav	10:59:29.3	+44:10:02.7	$r = 19.97$	(s) 0.05	Slow 2MASX
	ZTF18aavrhqs	11:58:09.5	+63:45:34.6	$r = 19.99$	Orphan	Slow
	ZTF18aawmwwk	10:35:26.5	+65:22:34.3	$r = 19.99$	(p) 0.18	Slow SDSS
	ZTF18aawwbwm	08:16:44.9	+35:34:13.1	$r = 19.79$	(p) 0.15	Slow SDSS
	ZTF18aawmjru	08:39:11.3	+44:01:53.6	$r = 18.43$	(p) 0.44	Slow SDSS
	ZTF18aawmigr	08:48:01.7	+29:13:51.9	$r = 19.63$	(s) 0.1	Slow 2MASX
GRB 180626C	ZTF18aauebur	19:48:49.1	+46:30:36.1	$r = 18.85$	Stellar	CV multiple previous bursts
GRB 180715B	ZTF18aamwzlv	13:06:44.5	+68:59:52.9	$r = 18.50$	(s) 0.1	Slow
	ZTF18abhbevp	14:21:00.8	+72:11:43.8	$g = 20.63$	⋯	Slow
	ZTF18abhbpkm	16:02:36.7	+70:47:05.1	$g = 21.24$	⋯	Slow
	ZTF18abhhjyd	13:02:32.0	+75:16:49.4	$g = 20.43$	⋯	AGN Milliquas
	ZTF18abhbgan	15:43:18.8	+72:05:24.8	$g = 21.22$	Orphan	Slow
	ZTF18abhbfoi	13:24:34.0	+70:56:47.5	$g = 21.12$	(s)1.2	AGN Milliquas and PS1
	ZTF18abhbcjy	14:20:50.3	+73:25:40.5	$g = 20.78$	⋯	Slow
	ZTF18abhaogg	13:42:45.4	+74:19:38.3	$r = 20.38$	Orphan	Slow
	ZTF18abhbamj	15:26:58.7	+72:02:17.8	$r = 21.27$	Orphan	Slow
	ZTF18abhawjn	13:31:27.3	+66:46:45.4	$g = 20.69$	(s) 0.4	AGN Milliquas
	ZTF18abharzk	13:41:09.0	+70:43:06.8	$r = 21.30$	⋯	Slow
	ZTF18abhbckn	12:49:53.8	+73:02:00.5	$r = 20.93$	(s) 0.00541	Slow CLU
	ZTF18abhbfqf	13:16:00.2	+69:37:24.1	$r = 19.80$	(s) 0.11	SN Ia-91T P200
	ZTF18aauhpyb	13:21:45.4	+70:55:59.8	$g = 19.67$	Stellar	CV multiple bursts P60
GRB 180913A	ZTF18abvzgms	23:37:50.5	+47:53:21.2	$g = 21.29$	(p) 0.35	Flat evolution SDSS
	ZTF18abwiios	23:12:14.0	+39:27:50.6	$g = 22.04$	⋯	Flat evolution
	ZTF18abvzfgy	23:16:15.2	+43:31:59.3	$g = 20.98$	(s) 0.04	SN Ic LDT
	ZTF18abvzjwk	22:30:32.4	+39:50:14.6	$g = 21.70$	⋯	Flat evolution
	ZTF18abvwhkl	23:05:44.1	+45:32:34.8	$r = 21.44$	⋯	Flat evolution 3 points
	ZTF18abvucnv	22:31:31.9	+39:30:03.7	$r = 21.15$	Stellar	Star flare
	ZTF18abwiitm	23:15:27.6	+39:57:10.5	$g = 21.71$	⋯	Slow AGN WISE
	ZTF18abvubdm	22:58:28.4	+47:06:03.8	$g = 21.01$	⋯	Slow evolution nice lc
	ZTF18abvzsld	00:15:57.1	+49:28:51.0	$g = 21.50$	Stellar	Flat evolution
	ZTF18abwiivr	22:52:15.8	+37:22:29.4	$g = 21.73$	Stellar	Slow evolution
	ZTF18abvzmtm	23:55:13.0	+48:21:37.8	$g = 21.65$	⋯	Slow
GRB 181126B	ZTF18achtkfy	06:54:02.6	+37:04:28.6	$g = 19.69$	Orphan	Slow
	ZTF18achflqs	04:41:09.4	+23:53:24.9	$r = 20.20$	(p) 0.38	Flat evolution SDSS
	ZTF18acrkcxa	04:55:02.5	+22:40:43.4	$r = 20.85$	Stellar	Flare Keck LRIS
	ZTF18acrkkpc	06:23:15.5	+10:19:22.6	$r = 20.17$	(s) 0.061	SN II Keck LRIS
	ZTF18aadwfrc	06:17:18.0	+50:29:03.3	$r = 19.65$	(s) 0.04	SN Ia-02cx Keck LRIS
	ZTF18acrfond	03:59:26.9	+24:35:20.4	$r = 10.13$	(s) 0.117	SN Ia Keck LRIS
	ZTF18acrfymv	06:18:01.1	+44:10:52.7	$g = 20.82$	(s) 0.072	SN Ic-BL Keck LRIS
	ZTF18acptgzz	04:33:32.4	-01:38:51.1	$r = 19.56$	(s) 0.096	SN Ia Keck LRIS
	ZTF18acbyrll	05:55:28.6	+29:28:20.3	$r = 19.34$	⋯	Slow evolution
	ZTF18acrewzd	04:41:17.2	-01:46:07.5	$g = 20.74$	(s) 0.13	SN Ia Keck LRIS
GRB 200514B	ZTF20aazpphd	16:10:51.5	+27:09:42.0	$r = 19.6$	⋯	Slow LCO
	ZTF20aazppnv	15:52:34.5	+25:34:35.3	$r = 21.1$	(p) 0.17	Slow LCO
	ZTF20aazprjq	15:34:05.1	+43:19:47.5	$r = 21.3$	(p) 0.23	Slow LCO
	ZTF20aazptlp	15:16:01.8	+48:46:29.7	$r = 21.5$	(p) 0.40	Slow LCO
	ZTF20aazptnn	15:49:11.2	+47:16:19.0	$r = 21.6$	(p) 0.26	Slow LCO
	ZTF20aazpnst	16:56:23.7	+34:27:55.9	$r = 22.0$	(p) 0.19	Slow LCO
	ZTF20aazpofi	15:47:43.0	+46:58:51.4	$r = 21.5$	(p) 0.46	Slow LCO
	ZTF20aazplwp	14:16:04.0	+41:10:02.1	$r = 21.6$	⋯	Slow LCO
	ZTF20aazqlgx	15:04:21.8	+34:37:33.4	$r = 22.3$	(p) 0.35	Slow LCO

Table 4
(Continued)

GRB Trigger	ZTF Name	R.A.	Decl.	Discovery Magnitude	Redshift	Rejection Criteria
	ZTF20aazphye	15:42:37.8	+41:42:04.7	$r = 21.6$	(p) 0.26	Slow LCO
	ZTF20aazpnxd	15:43:43.5	+48:23:10.6	$r = 21.6$	⋯	Slow LCO
	ZTF20aazpkri	14:42:55.7	+48:33:19.7	$r = 21.3$	⋯	Slow LCO
	ZTF20aazqndp	14:31:17.0	+50:29:35.8	$r = 22.1$	(s) 0.03	Slow LCO
	ZTF20aazqpps	15:28:57.3	+41:18:35.0	$r = 21.6$	(s) 0.2	Slow LCO
GRB 210510A	ZTF21abaytuk	13:48:49.8	+35:32:13.0	$g = 21.76$	(s) 0.8970	AGN Keck LRIS

Note. The spectroscopic (s) or photometric (p) redshifts of the respective host galaxies are listed as well. The photometric slow evolution of some candidates was used as a rejection criteria when the object presents a variation on its magnitude smaller than 0.3 mag day^{-1}. We mention the facility (P200, P60, Keck LRIS, LDT), or survey (SDSS, the Census of the Local Universe (CLU; Cook et al. 2019), the 2MASS Extended source (2MASX; Skrutskie et al. 2006), WISE, Milliquas) that allowed us to reject the source or pinpoint the redshift of the putative host galaxy.

magnitude of the source at different times (see below for the models used). `simsurvey` uses the ZTF logs to determine if the simulated source was in an observed ZTF field and whether the transient would have been detected given the upper limits of that ZTF field.

One of the driving features of an afterglow model is its isotropic-equivalent energy, $E_{\rm iso}$, as it sets the luminosity of the burst and hence its magnitude and light curve. The information provided by the Fermi-GBM gamma-ray detections does not give insights on the distance to the event or the energies associated with the SGRBs. For this reason, and to get a sense of the $E_{\rm iso}$ associated with each burst, we take two approaches: using the gamma-ray energy peak, $E_{\rm peak}$, and the average kinetic isotropic energy, $E_{K,\rm iso}$ to estimate $E_{\rm iso}$. First, we assume that our population of SGRBs follows the isotropic-energy ($E_{\rm iso}$)–rest-frame peak energy (E_z, p) relationship (see Equation (1)), postulated in Equation (2) of Tsutsui et al. (2013)

$$E_{\rm iso} = 10^{52.4\pm0.2}\ {\rm erg}\left(\frac{E_{z,p}}{774.5\ {\rm keV}}\right)^{1.6\pm0.3}. \quad (1)$$

This relationship requires the peak energies of the bursts, $E_{\rm p}$, which can be obtained by fitting a Band model (Band et al. 1993) to the gamma-ray emission over the duration of the burst. The results of this modeling are usually listed in the public GBM catalog (von Kienlin et al. 2020) and online.[50] The compilation of $E_{\rm p}$ for our SGRBs sample is listed in Table 1.

The energies that result from this transformation are usually larger than the energies derived for previous SGRB afterglows. For this reason, we additionally use the average kinetic isotropic energy, $E_{K,\rm iso}$, presented in Fong et al. (2015) as a representative value for $E_{\rm iso}$. Particularly, for this second $E_{\rm iso}$ approach, we assume $E_{K,\rm iso} \sim E_{\rm iso} = 2.9 \times 10^{51}$ erg.

We used the python module `afterglowpy` (Ryan et al. 2020) to generate afterglow light-curve templates. Due to the nature of the relativistic jet, we constrained the viewing angle to $\theta < 20°$. We chose a Gaussian jet and fixed other `afterglowpy` parameters to standard values based on the mean values derived in Fong et al. 2015: a circumburst density of $5.2 \times 10^{-3}\ {\rm cm}^{-3}$, the electron energy distribution index $p = 2.43$, as well as the fraction of shock energy imparted to electrons, $\epsilon_E = 0.1$, and to the magnetic field, $\epsilon_B = 0.01$. For $E_{\rm iso}$ we used the relation in Equation (1) and the mean $E_{K,\rm iso}$ mentioned in the paragraph above. Additionally for $E_{\rm iso}$ as a function of $E_{z,p}$, we took the gamma-ray $E_{z,p} = E_p(1+z)$, with the redshift varying for each simulated source.

We feed `simsurvey` light curves generated with `afterglowpy` assuming the two separate $E_{\rm iso}$ distributions described above. We note that these two approaches are based on conclusions drawn from Swift bursts, since the bulk of the SGRB afterglow knowledge comes from Swift bursts. We calculated the efficiency as a function of redshift by taking the ratio of sources detected twice over the number of generated sources within a redshift volume. We require two detections as our ToO strategy relies on at least two data points.

The efficiencies vary depending on a few factors. The total coverage and the limiting magnitude of the observations limit the maximum efficiency, which then decays depending on the associated $E_{\rm iso}$. For larger energies, the decay is smoother. In the top panel of Figure 9, we show the efficiencies for the nine GRBs that had no discovered counterpart. We exclude GRB 200826A as the energies used to model the afterglow follow the SGRB energy distribution, while GRB 200826A was proven to be part of the LGRB population. The energies derived from the Tsutsui et al. (2013) relationship are larger than the mean $E_{K,\rm iso}$ derived from Fong et al. (2015). This increases the efficiencies at larger redshifts assuming the Tsutsui et al. 2013 relationship, as the transients are intrinsically more energetic.

For both of the energies used, we calculate the joint probability of non-detection by taking the product of the SGRB ToO efficiencies as a function of redshift. Similar to the analysis in Kasliwal et al. (2020), we define

$$(1 - {\rm CL}) = \prod_{i=0}^{N} (1 - p_i) \quad (2)$$

with CL as the credible level and p_i the efficiency of the i*th* burst as a function of redshift. We show in the bottom panel of Figure 9 the result for the afterglows with energies following Tsutsui et al. (2013) (blue) and Fong et al. (2015) (yellow). The lower energies associated with Fong et al. 2015 afterglows only allow us to probe the space up to $z = 0.16$, considering a CL = 0.9, while SGRBs with energies following the $E_{\rm iso} - E_{z,p}$ relationship can be probed as far as $z = 0.4$. To look into the prospects of the SGRB ToO campaign, we model a scenario with 21 additional ToO campaigns, each with a median efficiency based on the results presented here. These results are shown as dashed lines in Figure 9, and show that for $E_{\rm iso} \sim E_{K,\rm iso}$, the improvement after thirty ToOs can only expand our searches (i.e., CL=0.9) up to $z = 0.2$, while if the GRBs follow the $E_{\rm iso} - E_{z,p}$ relationship, our horizon expands to $z = 0.7$.

[50] https://heasarc.gsfc.nasa.gov/W3Browse/fermi/fermigbrst.html

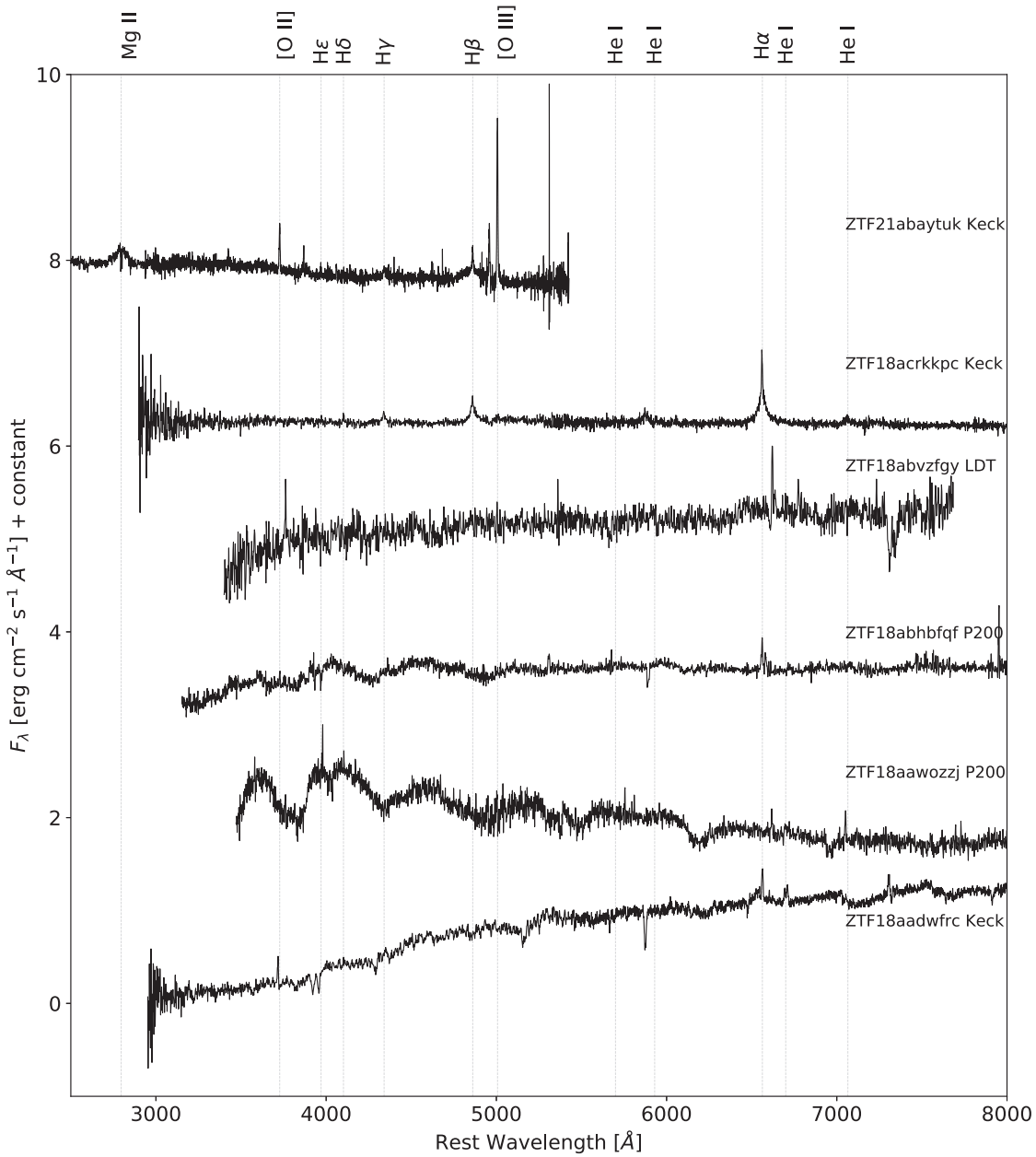

Figure 6. The spectra of some representative candidates. The spectrum of transient ZTF18aadwfrc was taken with the LRIS at the Keck Observatory and was classified as an SN Ia at $z = 0.04$. Similarly, the spectra of ZTF18acrkkpc and ZTF21abaytuk come from Keck as well, and were classified as an SN II at $z = 0.061$ and as an AGN at $z = 0.89$, respectively. We used the DBSP at P200 to acquire spectra of ZTF18aawozzj and ZTF18abhbfqf, two SN Ia at redshift $z = 0.095$ and $z = 0.11$, respectively. Last, the spectrum of ZTF18abvzfgy was obtained with the DeVeny Spectrograph at the LDT and, using `dash`, we classified it as a SN Ic at $z = 0.04$. For reference, we show the hydrogen, helium, magnesium, and some oxygen lines as vertical lines.

Finally, when comparing our limits to the redshift distribution of SGRB afterglows found in the literature (Fong et al. 2015) (green histogram in Figure 9), our searches show that we are probing (and could probe) volumes that contain 10%–40% of the observed afterglows, depending on the $E_{\rm iso}$ assumption.

7. Proposed Follow-up Strategy

The current ToO strategy aims for two consecutive exposures in two different filters, prioritizing the color of the source as the main avenue to discriminate between sources. This helps confirming the nature of the transient as an extragalactic source. In some cases, it can lead to problems as the source might not be detected at shorter wavelengths, due to either the extinction along the line of sight or its intrinsically fainter brightness. If there is no second detection at shorter wavelengths, there is the risk of ignoring a potential counterpart as a single detection can be confused as a slow-moving object or an artifact. The standard strategy considers a second night of ZTF observations in the same two filters, to measure the magnitude and color evolution. However, a number of sources did not have a second detection in the same filter after the second night, impeding the measurement of the decline rate. For these two reasons, for afterglow searches with ZTF (and possibly other instruments with similar limiting magnitudes), it is more informative to observe the region at least twice in the same filter during the first night. By separating the two same-filter epochs by at least $2\sigma \times 24/\alpha$, where σ is the typical error

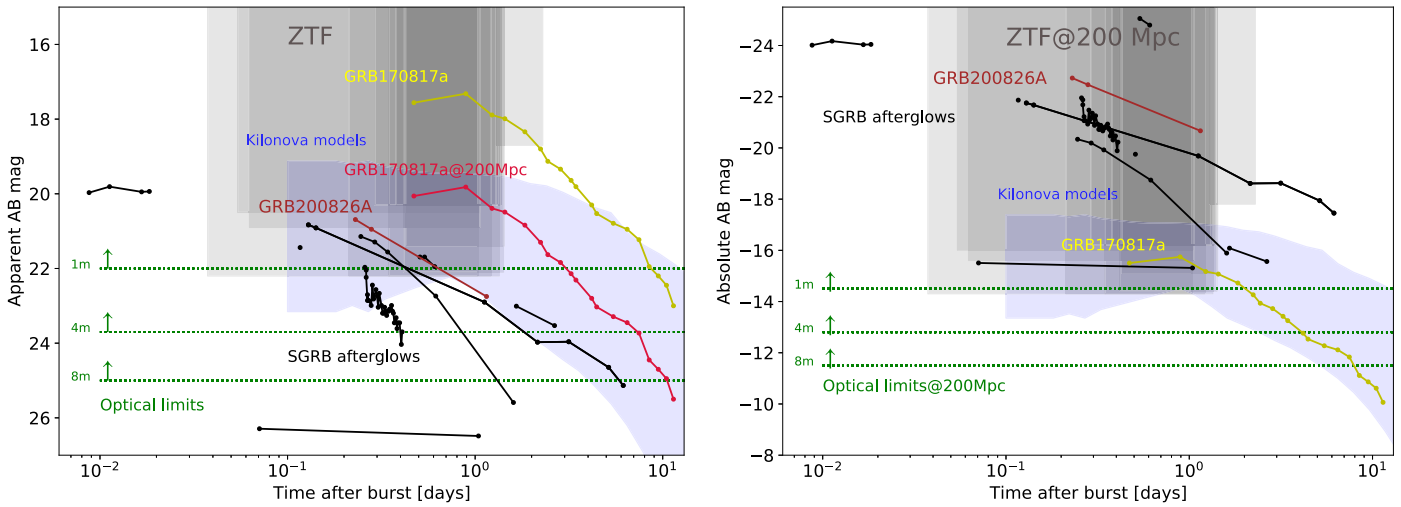

Figure 7. Left: the light curves (black) of the optical counterparts of SGRBs with known redshift listed in Fong et al. (2015). The yellow light curve is the GW170817 light curve and the red line is the GW170817 light curve scaled to a distance of 200 Mpc. Each of the ZTF search windows occupies a gray region, limited by the median limiting magnitude and the time window in which the search took place. The brown light curve is the afterglow of GRB 200826A (Ahumada et al. 2021) and the blue-shaded region represents the region that the KN models (Bulla 2019; Dietrich et al. 2020) occupy when scaled to 200 Mpc. The green-dotted lines represent the typical optical limits of imagers mounted at different telescopes, while the size of the telescope is annotated as a label in the plot. Right: the absolute magnitude of the same data plotted in the left panel. We compare their absolute magnitudes to the ZTF magnitude limits, scaled to a fiducial distance of 200 Mpc. Similarly, the green-dotted lines show the optical limits of different facilities, ranging in size, at 200 Mpc.

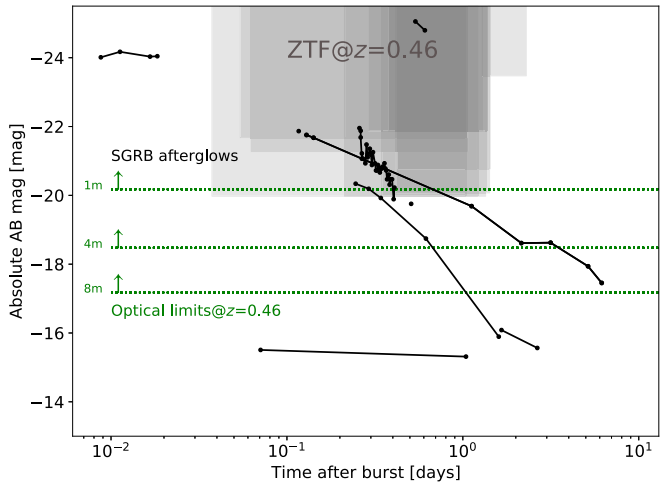

Figure 8. The absolute magnitude (black) of the optical counterparts of SGRBs with known redshift listed in Fong et al. (2015). Each of the ZTF search windows occupies a gray region, limited by the median limiting magnitude and the time window in which the search took place. The median limiting magnitudes are scaled to the median SGRB redshift of $z = 0.47$. The green-dotted lines represent the typical optical limits of imagers mounted at different telescopes, while the size of the telescope is annotated as a label in the plot. These limits are also scaled to the median SGRB redshift of at $z = 0.47$.

of the observations and α is the power-law index of the afterglow decline, we can possibly measure the decay rate of sources, or at least set a lower limit for α. For ZTF, two epochs separated by 6 hr would suffice for afterglows with a typical $\alpha \sim 1$, assuming $\sigma = 0.12$.

This scenario is unlikely to happen often, as it requires that the region is visible during the entire night and that the night is long enough to allow for two visits separated by a number of hours. In any case, the standard ToO strategy for the second night of observation (two visits in two different filters) should help determine the color and magnitude evolution.

For the third day of follow-up, there will be two kinds of candidates: (a) confirmed fast-fading transients, and (b) transients with unconstrained evolution, that likely only have data for the first night. For (a) it is important to get spectra as soon as possible before the transients fade below the spectroscopic limits. Ideally, observations in other wavelengths should be triggered to cement the classification and begin the characterization of the transient. For candidates in situation (b), the fast evolution of the transients requires the use of larger facilities. From our experience, this is feasible as only a handful of candidates will fall in this category. In both cases, (a) and (b), photometric follow-up using facilities different than ZTF are needed, as any afterglow detected by ZTF will likely not be detectable three days after the burst. In Figure 10 we show the magnitude distribution of all the transients that `simsurvey` detected, independent of redshift, as a function of how many days passed after the burst. This figure illustrates the need for other telescopes to monitor the evolution of the transient, as for example, only ∼30% of the transients that we can detect with ZTF will be brighter than $r = 22$ mag. Additionally, Figure 10 shows that spectroscopy of the sources becomes harder after day 2, as only 20% of the detected transients will be brighter than $r = 21.5$ mag.

Since spectroscopic data will be challenging to acquire for faint sources, the panchromatic follow-up, from radio to X-rays, will help to confirm the classification of the transient.

8. Conclusions

During a period of ∼2 yr, a systematic, extended and deep search for the optical counterparts to Fermi-GBM SGRBs has been performed employing the Zwicky Transient Facility. The ZTF observations of 10 events followed up are listed in Table 3 and no optical counterpart has yet been associated with a compact binary coalescence. However, our ToO strategy led to the discovery of the optical counterpart to GRB 200826A, which was ultimately revealed as the shortest-duration LGRB found to date (Ahumada et al. 2021).

This experiment complements previous studies (Singer et al. 2013, 2015; Coughlin et al. 2019a), and demonstrates the

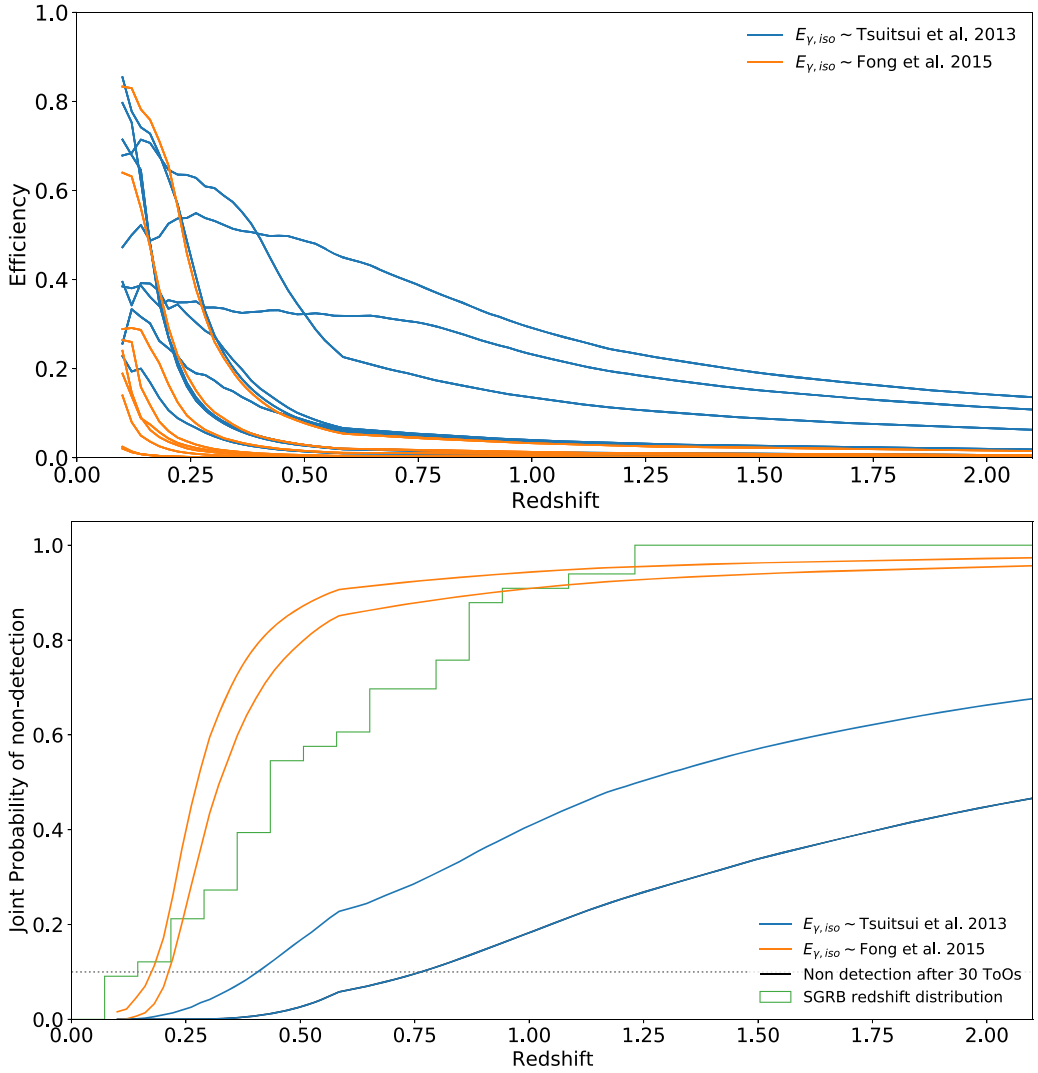

Figure 9. (top) The individual efficiency for each SGRB trigger. The blue curves are based on the $E_{\rm iso}$ derived from the Band model $E_{\rm p}$ and Equation (1), while the yellow curves are the efficiencies assuming all GRBs have the same $E_{\rm iso}$ as the mean $E_{K,\rm iso}$ from Fong et al. (2015). (bottom) The solid lines represent the joint probability of non-detection using the 9 SGRB triggers with no optical counterparts. We adopt the same color coding as in the top plot, meaning blue for the $E_{\rm iso}$ as a function of $E_{\rm p}$ and yellow for $E_{\rm iso}$ as the mean $E_{K,\rm iso}$ from Fong et al. 2015. The dashed line represent the joint probability of non-detection after 30 ToOs, assuming an efficiency equal to the median efficiency of the ToOs presented. We show the cumulative redshift distribution for SGRBs as a green line. The gray dotted line shows the CL = 0.9 level, at which the joint probability of non-detection is $1 - {\rm CL} = 0.1$.

feasibility of studying the large sky areas derived from Fermi-GBM by exploiting the wide field of view of ZTF. The average coverage was ~ 60% of the localization regions, corresponding to ~950 deg^2. The average amount of alerts in the targeted regions of the sky was over 20,000, and we were able to reduce this figure to no more than 20 candidates per trigger. Thanks to the high cadence of ZTF we were able to achieve a median reduction in alerts of 0.03%. The effectiveness of the filtering criteria is comparable with the median reduction reached in Singer et al. (2015), even when the areas covered are almost orders of magnitude larger. The iIPTF search for the optical counterparts to the long gamma-ray burst GRB 130702A covered 71 deg^2 and yielded 43 candidates (Singer et al. 2013).

This campaign has utilized ZTF capabilities to rapidly follow up the SGRB trigger, which has allowed us to explore the magnitude space and set constraints on SGRB events. The average depth for ZTF 300 s exposures is $r \sim 20.8$ which has allowed us to look for SGRB afterglows and GW170817-like KNe. From Figure 10, it can be seen that future follow-ups

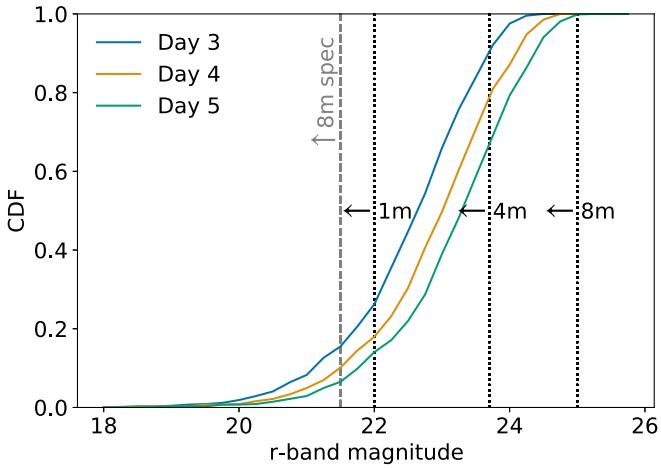

Figure 10. The magnitude cumulative distribution of the sources detected using `simsurvey` as a function of the days after the burst. This distribution contains all the sources detected up to $z = 2$. The photometric and spectroscopic limits of different facilities are shown as dotted vertical lines.

would benefit both from a more rapid response and longer exposures.

By using computational tools like `afterglowpy` and `simsurvey`, we have quantified the efficiency of our ToO triggers. The ZTF efficiency drops quickly as the transient is located at further distances, and the magnitude limits only allow for detections up to $z = 0.4$, for energies following the Tsutsui et al. (2013) relation and $z = 0.16$ for bursts with energies equal to the mean $E_{\rm iso}$ found by Fong et al. (2015), for a CL = 0.9. Furthermore, when repeating the experiment 21 times (to complete 30 ToOs) and assuming a median efficiency $p_{\rm med}$ for each new event, the horizons of our searches increase to $z = 0.2$ and 0.72, respectively.

Additionally, our simulations show that ZTF is no longer effective at following up afterglows after three days following the burst. The fast-fading nature of these transients requires deeper observations, and spectroscopic and panchromatic observations are helpful to reveal the nature of the candidates. Ideally, at least two observations in the same filter should be taken during the first night of observation, as afterglows and KNe fade extremely rapidly and they might not be observable 48 hr after the burst. With this strategy, we can hope to find another counterpart.

Based on observations obtained with the Samuel Oschin Telescope 48 inch and the 60 inch Telescope at the Palomar Observatory as part of the Zwicky Transient Facility project. ZTF is supported by the National Science Foundation under Grants No. AST-1440341 and AST-2034437 and a collaboration including current partners Caltech, IPAC, the Weizmann Institute for Science, the Oskar Klein Center at Stockholm University, the University of Maryland, Deutsches Elektronen-Synchrotron and Humboldt University, the TANGO Consortium of Taiwan, the University of Wisconsin at Milwaukee, Trinity College Dublin, Lawrence Livermore National Laboratories, IN2P3, University of Warwick, Ruhr University Bochum, Northwestern University and former partners the University of Washington, Los Alamos National Laboratories, and Lawrence Berkeley National Laboratories. Operations are conducted by COO, IPAC, and UW. This work was supported by the GROWTH (Global Relay of Observatories Watching Transients Happen) project funded by the National Science Foundation under PIRE grant No. 1545949. GROWTH is a collaborative project among California Institute of Technology (USA), University of Maryland College Park (USA), University of Wisconsin Milwaukee (USA), Texas Tech University (USA), San Diego State University (USA), University of Washington (USA), Los Alamos National Laboratory (USA), Tokyo Institute of Technology (Japan), National Central University (Taiwan), Indian Institute of Astrophysics (India), Indian Institute of Technology Bombay (India), Weizmann Institute of Science (Israel), The Oskar Klein Centre at Stockholm University (Sweden), Humboldt University (Germany), Liverpool John Moores University (UK) and University of Sydney (Australia). T.A. and H.K. thank the LSSTC Data Science Fellowship Program, which is funded by LSSTC, NSF Cybertraining grant #1829740, the Brinson Foundation, and the Moore Foundation; their participation in the program has benefited this work. M.M.K. acknowledges generous support from the David and Lucille Packard Foundation. M.W.C. acknowledges support from the National Science Foundation with grant Nos. PHY-2010970 and OAC-2117997. S.A. acknowledges support from the GROWTH PIRE grant No. 1545949. A.S.C. acknowledges support from the G.R.E.A.T research environment, funded by *Vetenskapsrådet*, the Swedish Research Council, project number 2016-06012. M.B. acknowledges support from the Swedish Research Council (Reg. no. 2020-03330). S.R. acknowledges support by the Helmholtz Weizmann Research School on Multimessenger Astronomy, funded through the Initiative and Networking Fund of the Helmholtz Association, DESY, the Weizmann Institute, the Humboldt University of Berlin, and the University of Potsdam. ECK acknowledges support from the G.R.E.A.T research environment funded by *Vetenskapsrådet*, the Swedish Research Council, under project number 2016-06012, and support from The Wenner-Gren Foundations. P.R. acknowledges the support received from the Agence Nationale de la Recherche of the French government through the program Investissements d'Avenir" (16-IDEX-0001 CAP 20-25) The material is based on work supported by NASA under award No. 80GSFC17M0002. Based on observations obtained at the international Gemini Observatory, a program of NSF's NOIRLab, which is managed by the Association of Universities for Research in Astronomy (AURA) under a cooperative agreement with the National Science Foundation on behalf of the Gemini Observatory partnership: the National Science Foundation (United States), National Research Council (Canada), Agencia Nacional de Investigación y Desarrollo (Chile), Ministerio de Ciencia, Tecnología e Innovación (Argentina), Ministério da Ciência, Tecnologia, Inovações e Comunicações (Brazil), and Korea Astronomy and Space Science Institute (Republic of Korea). The observations were obtained as part of Gemini Director's Discretionary Program GN-2021A-Q-102. The Gemini data were processed using DRAGONS (Data Reduction for Astronomy from Gemini Observatory North and South). This work was enabled by observations made from the Gemini North telescope, located within the Maunakea Science Reserve and adjacent to the summit of Maunakea. We are grateful for the privilege of observing the Universe from a place that is unique in both its astronomical quality and its cultural significance. The ZTF forced-photometry service was funded under the Heising-Simons Foundation grant No. 12540303 (PI: Graham). These results also made use of Lowell Observatory's Lowell Discovery Telescope (LDT), formerly the Discovery Channel Telescope. Lowell operates the LDT in partnership with Boston University, Northern Arizona University, the University of Maryland and the University of Toledo. Partial support of the LDT was provided by Discovery Communications. LMI was built by Lowell Observatory using funds from the National Science Foundation (AST-1005313). The Liverpool Telescope is operated on the island of La Palma by Liverpool John Moores University in the Spanish Observatorio del Roque de los Muchachos of the Instituto de Astrofisica de Canarias with financial support from the UK Science and Technology Facilities Council. SED Machine is based upon work supported by the National Science Foundation under grant No. 1106171. GIT is a 70 cm telescope with a $0\overset{\circ}{.}7$ field of view, set up by the Indian Institute of Astrophysics (IIA) and the Indian Institute of Technology Bombay (IITB) with funding from DST-SERB and IUSSTF. It is located at the Indian Astronomical Observatory, operated by IIA. We acknowledge funding by the IITB alumni batch of 1994, which partially supports operations of the telescope. Telescope technical details are available at https://sites.google.com/view/growthindia/.

Facilities: *Fermi*-GBM, ZTF/PO:1.2 m, P60, P200, KPED, LCOGT, Gemini, LDT, Keck, LT, GIT.

Software: `ipython` (Pérez and Granger 2007), `jupyter` (Kluyver et al. 2016), `matplotlib` (Hunter 2007), `python` (Van Rossum & Drake 2009), `NumPy` (Harris et al. 2020), `afterglowpy` (Ryan et al. 2020), `simsurvey` (Feindt et al. 2019), `pysedm` (Rigault et al. 2019), `SNID` (Blondin & Tonry 2007), `PyRAF-dbsp` (Bellm & Sesar 2016) , `DRAGONS` Labrie et al. 2019, `HOTPANTS` (Becker 2015), `Force-PhotZTF` (Yao et al. 2019), `ZTF FP` (Masci et al. 2019).

ORCID iDs

Tomás Ahumada https://orcid.org/0000-0002-2184-6430
Shreya Anand https://orcid.org/0000-0003-3768-7515
Michael W. Coughlin https://orcid.org/0000-0002-8262-2924
Igor Andreoni https://orcid.org/0000-0002-8977-1498
Erik C. Kool https://orcid.org/0000-0002-7252-3877
Harsh Kumar https://orcid.org/0000-0003-0871-4641
Simeon Reusch https://orcid.org/0000-0002-7788-628X
Ana Sagués-Carracedo https://orcid.org/0000-0002-3498-2167
Robert Stein https://orcid.org/0000-0003-2434-0387
S. Bradley Cenko https://orcid.org/0000-0003-1673-970X
Mansi M. Kasliwal https://orcid.org/0000-0002-5619-4938
Leo P. Singer https://orcid.org/0000-0001-9898-5597
Varun Bhalerao https://orcid.org/0000-0002-6112-7609
Mattia Bulla https://orcid.org/0000-0002-8255-5127
Eric Burns https://orcid.org/0000-0002-2942-3379
Matthew J. Graham https://orcid.org/0000-0002-3168-0139
David L. Kaplan https://orcid.org/0000-0001-6295-2881
Daniel Perley https://orcid.org/0000-0001-8472-1996
Mouza Almualla https://orcid.org/0000-0002-4694-7123
Joshua S. Bloom https://orcid.org/0000-0002-7777-216X
Kishalay De https://orcid.org/0000-0002-0786-7307
Pradip Gatkine https://orcid.org/0000-0002-1955-2230
Anna Y. Q. Ho https://orcid.org/0000-0002-9017-3567
Viraj Karambelkar https://orcid.org/0000-0003-2758-159X
Albert K. H. Kong https://orcid.org/0000-0002-5105-344X
Yuhan Yao https://orcid.org/0000-0001-6747-8509
G. C. Anupama https://orcid.org/0000-0003-3533-7183
Sudhanshu Barway https://orcid.org/0000-0002-3927-5402
Ryosuke Itoh https://orcid.org/0000-0002-1183-8955
Eric C. Bellm https://orcid.org/0000-0001-8018-5348
Christoffer Fremling https://orcid.org/0000-0002-4223-103X
Russ R. Laher https://orcid.org/0000-0003-2451-5482
Ashish A. Mahabal https://orcid.org/0000-0003-2242-0244
Reed L. Riddle https://orcid.org/0000-0002-0387-370X
Ben Rusholme https://orcid.org/0000-0001-7648-4142
Roger Smith https://orcid.org/0000-0001-7062-9726
Jesper Sollerman https://orcid.org/0000-0003-1546-6615
Elisabetta Bissaldi https://orcid.org/0000-0001-9935-8106
Christian Malacaria https://orcid.org/0000-0002-0380-0041
Oliver Roberts https://orcid.org/0000-0002-7150-9061

References

Abbott, B. P., Abbott, R., Abbott, T.D., et al. 2017a, PhRvL, 119, 161101
Abbott, B. P., Abbott, R., Abbott, T. D., et al. 2017b, ApJL, 848, L13
Abbott, B. P., Abbott, R., Abbott, T. D., et al. 2017c, PhRvL, 118, 221101
Abbott, B. P., Abbott, R., Abbott, T. D., et al. 2018, LRR, 21, 3
Ahumada, R., Allende Prieto, C., Almeida, A., et al. 2020a, ApJS, 249, 3
Ahumada, T., Kumar, H., Fremling, C., et al. 2020b, GCN, 29029, 1
Ahumada, T., Anand, S., Andreoni, I., et al. 2020, GCN, 27737, 1
Ahumada, T., Coughlin, M. W., Cenko, S. B., et al. 2018, GCN, 23515, 1
Ahumada, T., Singer, L. P., Anand, S., et al. 2021, NatAs, 5, 917
Almualla, M., Coughlin, M. W., Anand, S., et al. 2020, MNRAS, 495, 4366
Amati, L. 2021, NatAs, 5, 877
Anand, S., Andreoni, I., Ahumada, T., et al. 2021, GCN, 30005, 1
Anand, S., Coughlin, M. W., Kasliwal, M. M., et al. 2021, NatAs, 5, 46
Andreoni, I., Coughlin, M. W., Kool, E. C., et al. 2021, ApJ, 918, 63
Andreoni, I., Goldstein, D. A., Anand, S., et al. 2019, ApJL, 881, L16
Andreoni, I., Goldstein, D. A., Kasliwal, M. M., et al. 2020, ApJ, 890, 131
Andreoni, I., Kool, E. C., Carracedo, A. S., et al. 2020, ApJ, 904, 155
Arcavi, I., Hosseinzadeh, G., Howell, D. A., et al. 2017, Natur, 551, 64
Ascenzi, S., Coughlin, M. W., Dietrich, T., et al. 2019, MNRAS, 486, 672
Band, D., Matteson, J., Ford, L., et al. 1993, ApJ, 413, 281
Becker, A. 2015, HOTPANTS: High Order Transform of PSF ANd Template Subtraction, Astrophysics Source Code Library, ascl:1504.004
Bellm, E. C., Kulkarni, S. R., Graham, M. J., et al. 2019a, PASP, 131, 018002
Bellm, E. C., Kulkarni, S. R., Barlow, T., et al. 2019b, PASP, 131, 068003
Bellm, E. C., & Sesar, B. 2016, pyraf-dbsp: Reduction Pipeline for the Palomar Double Beam Spectrograph, Astrophysics Source Code Library, ascl:1602.002
Berger, E., Price, P. A., Cenko, S. B., et al. 2005, Natur, 438, 988
Bertin, E., & Arnouts, S. 1996, A&AS, 117, 393
Blagorodnova, N., Neill, J. D., Walters, R., et al. 2018, PASP, 130, 035003
Blondin, S., & Tonry, J. L. 2007, ApJ, 666, 1024
Bloom, J. S., Kulkarni, S. R., Djorgovski, S. G., et al. 1999, Natur, 401, 453
Bromberg, O., Nakar, E., Piran, T., & Sari, R. 2013, ApJ, 764, 179
Brown, T. M., Baliber, N., Bianco, F. B., et al. 2013, PASP, 125, 1031
Bulla, M. 2019, MNRAS, 489, 5037
Burns, E., Svinkin, D., Hurley, K., et al. 2021, ApJL, 907, L28
Cannizzo, J. K., & Gehrels, N. 2009, ApJ, 700, 1047
Cano, Z., Wang, S.-Q., Dai, Z.-G., & Wu, X.-F. 2017, AdAst, 2017, 8929054
Cenko, S. B., Coughlin, M. W., Ghosh, S., et al. 2018, GCN, 22969, 1
Chambers, K. C., Magnier, E. A., Metcalfe, N., et al. 2016, arXiv:1612.05560
Chatterjee, D., Nugent, P. E., Brady, P. R., et al. 2019, ApJ, 881, 128
Chornock, R., Berger, E., Kasen, D., et al. 2017, ApJL, 848, L19
Cook, D. O., Kasliwal, M. M., Van Sistine, A., et al. 2019, ApJ, 880, 7
Côté, B., Fryer, C. L., Belczynski, K., et al. 2018, ApJ, 855, 99
Coughlin, M. W., Ahumada, T., Cenko, B., et al. 2018a, GCN, 23379, 1
Coughlin, M. W., Ahumada, T., Anand, S., et al. 2019b, ApJL, 885, L19
Coughlin, M. W., Ahumada, T., Cenko, S. B., et al. 2019a, PASP, 131, 048001
Coughlin, M. W., Dekany, R. G., Duev, D. A., et al. 2019b, MNRAS, 485, 1412
Coughlin, M. W., Antier, S., Corre, D., et al. 2019c, MNRAS, 489, 5775
Coughlin, M. W., Cenko, S. B., Ahumada, T., et al. 2018b, GCN, 23324, 1
Coughlin, M. W., Singer, L. P., Ahumada, T., et al. 2018a, GCN, 22871, 1
Coughlin, M. W., Singer, L. P., Cenko, S. B., et al. 2018b, GCN, 22739, 1
Coughlin, M. W., Tao, D., Chan, M. L., et al. 2018, MNRAS, 478, 692
Coulter, D. A., Foley, R. J., Kilpatrick, C. D., et al. 2017, Sci, 358, 1556
Cowperthwaite, P. S., Berger, E., Villar, V. A., et al. 2017, ApJL, 848, L17
Cutri, R. M., Wright, E. L., Conrow, T., et al. 2013, Explanatory Supplement to the AllWISE Data Release Products
D'Avanzo, P. 2015, JHEAp, 7, 73
De, K., Hankins, M. J., Kasliwal, M. M., et al. 2020, PASP, 132, 025001
Dekany, R., Smith, R. M., Riddle, R., et al. 2020, PASP, 132, 038001
Dichiara, S., Troja, E., O'Connor, B., et al. 2020, MNRAS, 492, 5011
Dietrich, T., Coughlin, M. W., Pang, P. T. H., et al. 2020, Sci, 370, 1450
Drake, A., Djorgovski, S., Mahabal, A., et al. 2009, ApJ, 696, 870
Drout, M. R., Piro, A. L., Shappee, B. J., et al. 2017, Sci, 358, 1570
Duev, D. A., Mahabal, A., Masci, F. J., et al. 2019, MNRAS, 489, 3582
Duffell, P. C., & MacFadyen, A. I. 2015, ApJ, 806, 205
Evans, P. A., Cenko, S. B., Kennea, J. A., et al. 2017, Sci, 358, 1565
Feindt, U., Nordin, J., Rigault, M., et al. 2019, JCAP, 2019, 005
Flesch, E. W. 2019, arXiv:1912.05614
Fong, W., Berger, E., Margutti, R., & Zauderer, B. A. 2015, ApJ, 815, 102
Fong, W., Laskar, T., Rastinejad, J., et al. 2021, ApJ, 906, 127
Fong, W., Margutti, R., Chornock, R., et al. 2016, ApJ, 833, 151
Fremling, C., Sollerman, J., Taddia, F., et al. 2016, A&A, 593, A68
Gal-Yam, A., Fox, D., & MacFayden, A. 2006, Natur, 444, 1053
Goldstein, A., Fletcher, C., Veres, P., et al. 2020, ApJ, 895, 40
Goldstein, A., Veres, P., Burns, E., et al. 2017, ApJL, 848, L14
Goldstein, D. A., Andreoni, I., Nugent, P. E., et al. 2019, ApJL, 881, L7
Gompertz, B., Levan, A., Tanvir, N., et al. 2018, ApJ, 860, 62
Graham, M. J., Kulkarni, S., Bellm, E. C., et al. 2019, PASP, 131, 078001
Hamburg, R., Veres, P., & Meegan, C. 2018, GCN, 23057, 1
Harris, C. R., Millman, K. J., van der Walt, S. J., et al. 2020, Natur, 585, 357
Ho, A. Y. Q., Perley, D. A., Yao, Y., et al. 2022, arXiv:2201.12366

Hosseinzadeh, G., Cowperthwaite, P. S., Gomez, S., et al. 2019, ApJL, 880, L4
Hunter, J. D. 2007, CSE, 9, 90
Kasen, D., Metzger, B., Barnes, J., Quataert, E., & Ramirez-Ruiz, E. 2017, Natur, 551, 80, EP
Kasliwal, M., Cannella, C., Bagdasaryan, A., et al. 2019, PASP, 131, 038003
Kasliwal, M. M., Anand, S., Ahumada, T., et al. 2020, ApJ, 905, 145
Kasliwal, M. M., Nakar, E., Singer, L. P., et al. 2017, Sci, 358, 1559
Kilpatrick, C. D., Foley, R. J., Kasen, D., et al. 2017, Sci, 358, 1583
Klebesadel, R. W., Strong, I. B., & Olson, R. A. 1973, ApJL, 182, L85
Kluyver, T., Ragan-Kelley, B., Pérez, F., et al. 2016, in Positioning and Power in Academic Publishing: Players, Agents and Agendas, ed. F. Loizides & B. Scmidt (Netherlands: IOS Press), 87
Kotani, T., Kawai, N., Yanagisawa, K., et al. 2005, NCimC, 28, 755
Kouveliotou, C., Meegan, C. A., Fishman, G. J., et al. 1993, ApJ, 413, L101
Kumar, P., & Granot, J. 2003, ApJ, 591, 1075
Labrie, K., Anderson, K., Cárdenes, R., Simpson, C., & Turner, J. E. H. 2019, in ASP Conf. Ser., 523, Astronomical Data Analysis Software and Systems XXVII, ed. P. J. Teuben (San Francisco, CA: ASP), 321
Lattimer, J. M., & Schramm, D. N. 1974, ApJL, 192, L145
Law, N., Kulkarni, S., Dekany, R., et al. 2009, PASP, 121, 1395
Lazzati, D., López-Cámara, D., Cantiello, M., et al. 2017, ApJL, 848, L6
Li, L.-X., & Paczynski, B. 1998, ApJL, 507, L59
Lipunov, V., Kornilov, V., Krylov, A., et al. 2005, Ap, 48, 389
Lipunov, V., Gorbovskoy, E., Kornilov, V., et al. 2017, ApJL, 850, L1
MacFarlane, M. J., & Dunham, E. W. 2004, Proc. SPIE, 5489, 796
Mahabal, A., Rebbapragada, U., Walters, R., et al. 2019, PASP, 131, 038002
Masci, F. J., Laher, R. R., Rusholme, B., et al. 2019, PASP, 131, 018003
McCully, C., Hiramatsu, D., Howell, D. A., et al. 2017, ApJL, 848, L32
Meegan, C., Lichti, G., Bhat, P. N., et al. 2009, ApJ, 702, 791
Mészáros, P., & Rees, M. J. 1998, ApJL, 502, L105
Metzger, B. D., Giannios, D., Thompson, T. A., Bucciantini, N., & Quataert, E. 2011, MNRAS, 413, 2031
Metzger, B. D., Martínez-Pinedo, G., Darbha, S., et al. 2010, MNRAS, 406, 2650
Metzger, M., Djorgovski, S., Kulkarni, S., et al. 1997, Natur, 387, 878
Mong, Y., Ackley, K., Galloway, D., et al. 2021, MNRAS, 507, 5463
Mooley, K. P., Nakar, E., Hotokezaka, K., et al. 2017, Natur, 554, 207, EP
Morrissey, P., Conrow, T., Barlow, T. A., et al. 2007, ApJS, 173, 682
Muthukrishna, D., Parkinson, D., & Tucker, B. E. 2019, ApJ, 885, 85
Nagakura, H., Hotokezaka, K., Sekiguchi, Y., Shibata, M., & Ioka, K. 2014, ApJL, 784, L28
Nakar, E. 2007, PhR, 442, 166
Narayan, R., Paczynski, B., & Piran, T. 1992, ApJL, 395, L83
Nicholl, M., Berger, E., Kasen, D., et al. 2017, ApJL, 848, L18
Nordin, J., Brinnel, V., Van Santen, J., et al. 2019, A&A, 631, A147
O'Connor, B., Troja, E., Dichiara, S., et al. 2021, MNRAS, 502, 1279
Oke, J., Cohen, J., Carr, M., et al. 1995, PASP, 107, 375
Patterson, M. T., Bellm, E. C., Rusholme, B., et al. 2019, PASP, 131, 018001
Pérez, F., & Granger, B. E. 2007, CSE, 9, 21
Pian, E., D'Avanzo, P., Benetti, S., et al. 2017, Natur, 551, 67
Piran, T. 1999, PhR, 314, 575
Rastinejad, J. C., Fong, W., Kilpatrick, C. D., et al. 2021, ApJ, 916, 89
Rau, A., Kulkarni, S., Law, N., et al. 2009, PASP, 121, 1334
Reusch, S., Ahumada, T., Anand, S., et al. 2020a, GCN, 27745, 1
Reusch, S., Andreoni, I., Kumar, H., et al. 2020b, GCN, 28981, 1
Rhodes, L., Fender, R., Williams, D. R. A., & Mooley, K. 2021, MNRAS, 503, 2966
Rigault, M., Neill, J. D., Blagorodnova, N., et al. 2019, A&A, 627, A115
Rossi, A., Rothberg, B., Palazzi, E., et al. 2021, arXiv:2105.03829
Rossi, A., Stratta, G., Maiorano, E., et al. 2020, MNRAS, 493, 3379
Rosswog, S. 2015, IJMPD, 24, 1530012
Ryan, G., Van Eerten, H., Piro, L., & Troja, E. 2020, ApJ, 896, 166
Shappee, B. J., Simon, J. D., Drout, M. R., et al. 2017, Sci, 358, 1574
Singer, L. P., Cenko, S. B., Kasliwal, M. M., et al. 2013, ApJL, 776, L34
Singer, L. P., Kasliwal, M. M., Cenko, S. B., et al. 2015, ApJ, 806, 52
Skrutskie, M. F., Cutri, R. M., Stiening, R., et al. 2006, AJ, 131, 1163
Smartt, S. J., Chen, T.-W., Jerkstrand, A., et al. 2017, Natur, 551, 75, EP
Steele, I. A., Smith, R. J., Rees, P. C., et al. 2004, Proc. SPIE, 5489, 679
Stein, R., Reusch, S., & Necker, J. 2021, desy-multimessenger/nuztf: v2.4.1,, Zenodo, doi:10.5281/zenodo.5758176
Stein, R., Velzen, S. v., Kowalski, M., et al. 2021, NatAs, 5, 510
Stern, D., Assef, R. J., Benford, D. J., et al. 2012, ApJ, 753, 30
Svinkin, D., Golenetskii, S., Aptekar, R., et al. 2020, GCN, 27755, 1
Tachibana, Y., & Miller, A. A. 2018, PASP, 130, 128001
Tanvir, N. R., Levan, A. J., González-Fernández, C., et al. 2017, ApJL, 848, L27
Tonry, J. L. 2011, PASP, 123, 58
Troja, E., Castro-Tirado, A. J., Becerra González, J., et al. 2019, MNRAS, 489, 2104
Troja, E., Piro, L., van Eerten, H., et al. 2017, Natur, 551, 71, EP
Tsutsui, R., Yonetoku, D., Nakamura, T., Takahashi, K., & Morihara, Y. 2013, MNRAS, 431, 1398
Van Rossum, G., & Drake, F. L. 2009, Python 3 Reference Manual (Scotts Valley, CA: CreateSpace),
Vieira, N., Ruan, J. J., Haggard, D., et al. 2020, ApJ, 895, 96
von Kienlin, A., Meegan, C. A., Paciesas, W. S., et al. 2020, ApJ, 893, 46
Wijers, R. A. M. J., Rees, M. J., & Mészáros, P. 1997, MNRAS, 288, L51
Willingale, R., O'Brien, P. T., Osborne, J. P., et al. 2007, ApJ, 662, 1093
Woosley, S. E., & Bloom, J. S. 2006, ARA&A, 44, 507
Wright, E. L., Eisenhardt, P. R. M., Mainzer, A. K., et al. 2010, AJ, 140, 1868
Yao, Y., Miller, A. A., Kulkarni, S., et al. 2019, ApJ, 886, 152
Zackay, B., Ofek, E. O., & Gal-Yam, A. 2016, ApJ, 830, 27
Zhang, B. 2013, ApJL, 763, L22
Zhang, B. B., Liu, Z. K., Peng, Z. K., et al. 2021, NatAs, 5, 911
Zhang, Z. -B., & Choi, C. -S. 2008, A&Ap, 484, 293
Zhang, Z., Chen, D., & Huang, Y. 2012, ApJ, 755, 55
Zhu, J.-P., Yang, Y.-P., Zhang, B., Gao, H., & Yu, Y.-W. 2021, arXiv:2110.10468